AFRL-SR-BL-TR-00-

0020

# REPORT DOCUMENTATION PAGE



| 1. REPORT DATE (DD-MM-YYYY) | 2. REPORT TYPE | 3. DATES COVERED (From - To) |
|---|---|---|
| 05-01-00 | Final Technical Report | 01 Sept 96 - 31 Aug 99 |

**4. TITLE AND SUBTITLE**

DEPSCOR-95 Develpment of Nonlinear Optical Materials for Optical Parametric Oscillator and Frequency Conversion Applications in the Near- and Mid-Infrared

**5a. CONTRACT NUMBER**

F49620-96-1-0452

**5b. GRANT NUMBER**

**5c. PROGRAM ELEMENT NUMBER**

**5d. PROJECT NUMBER**

**5e. TASK NUMBER**

**5f. WORK UNIT NUMBER**

**6. AUTHOR(S)**

Halliburton, Larry E.
Giles, Nancy C.
Myers, Thomas H.

**7. PERFORMING ORGANIZATION NAME(S) AND ADDRESS(ES)**

Physics Department
West Virginia University
P.O. Box 6315 / Morgantown, WV 26506-6315

**8. PERFORMING ORGANIZATION REPORT NUMBER**

**9. SPONSORING/MONITORING AGENCY NAME(S) AND ADDRESS(ES)**

Air Force Office of Scientific Research
801 N. Randolph Street
Arlington, VA 22203

**10. SPONSOR/MONITOR'S ACRONYM(S)**

AFOSR/NE

**11. SPONSOR/MONITOR'S REPORT NUMBER(S)**

**12. DISTRIBUTION/AVAILABILITY STATEMENT**

Distribution unlimited.

**13. SUPPLEMENTARY NOTES**

**14. ABSTRACT**

Point defects and their associated optical absorption bands often limit the performance of tunable laser sources (i.e., optical parametric oscillators) operating in the near and mid-infrared. Near-edge absorption in $ZnGeP_2$ crystals and gray tracks in KTP crystals are examples of device limiting phenomena in commercially available materials, and both of these effects result from uncontrolled point defects introduced into the crystals during growth. This project identified and characterized the dominant defects in these materials. The experimental techniques employed were electron paramagnetic resonance (EPR), electron-nuclear double resonance (ENDOR), photoluminescence (PL), optical absorption, and Hall measurements. Information obtained from these studies is published and has been provided to our industrial partners where crystal growth procedures were modified in order to minimize the particular defects being identified in our spectroscopic studies. Our industrial partners were Sanders (a Lockheed Martin Company) in Nashua, NH. and Crystal Associates, Inc. in East Hanover, NJ. Specific studies included: platinum-, silicon-, and titanium-associated traps in KTP; the zinc vacancy and cation-antisite defects in $ZnGeP_2$; and Hall measurements of $CdGeAs_2$.

**15. SUBJECT TERMS**

nonlinear optical materials, tunable lasers, infrared countermeasures, point defects, optical absorption, electron paramagnetic resonance, KTP, ZnGeP2,CdGeAs2

| 16. SECURITY CLASSIFICATION OF: | | | 17. LIMITATION OF ABSTRACT | 18. NUMBER OF PAGES | 19a. NAME OF RESPONSIBLE PERSON |
|---|---|---|---|---|---|
| a. REPORT | b. ABSTRACT | c. THIS PAGE | | 71 | Larry E. Halliburton |
| | | | | | 19b. TELEPHONE NUMBER (Include area code) 304-293-3422, ext. 1442 |

**FINAL TECHNICAL REPORT**

**(Covering the Period from September 15, 1996 to September 14, 1999)**

TABLE OF CONTENTS



## I. EXECUTIVE SUMMARY

This document is the final technical report for work performed under Air Force Office of Scientific Research (AFOSR) Grant F49620-96-1-0452. The title of the project is "Development of Nonlinear Optical Materials for Optical Parametric Oscillator and Frequency Conversion Applications in the Near- and Mid-Infrared" and the Principal Investigators are Larry E. Halliburton, Nancy C. Giles, and Thomas Myers. The three PI's are faculty members in the Physics Department at West Virginia University. In this three-year research program, spectroscopic techniques were used to improve the quality of $ZnGeP_2$, $CdGeAs_2$, and $KTiOPO_4$ crystals. These nonlinear optical materials are important components of frequency agile laser systems operating in the near and mid-infrared regions of the electromagnetic spectrum. One immediate application of these materials is in infrared countermeasures for heat-seeking missiles. Another application involves the conversion of intense 1.064-μm infrared laser beams into 532-nm visible beams via second harmonic generation. Point defects in these nonlinear optical crystals are known to limit the high-power performance of the devices. Our research has focused on the identification, characterization, and removal of the responsible point defects and we have worked closely with our industrial partners, Sanders (a Lockheed Martin Company) in Nashua, NH and Crystal Associates in East Hanover, NJ. The experimental techniques employed in this project

have included electron paramagnetic resonance (EPR), electron-nuclear double resonance (ENDOR), photoluminescence (PL), optical absorption, and Hall measurements.

The dissertations, theses, publications, and presentations which resulted from this AFOSR project are listed below. Of particular note, Scott Setzler completed all of the requirements for his Ph.D. in Physics in March of 1998 at West Virginia University and is now employed as a permanent staff scientist by our industrial partner Lockheed Martin in Nashua, NH. Dr. Setzler's dissertation, written on results obtained while he was working on this AFOSR project, describe important results on the origins of gray tracking in KTP crystals. The training made possible by the present grant led directly to this employment opportunity in the aerospace industry. A second student, Kevin Stevens, completed all of the requirements for his Ph.D. in Physics in December of 1999. Dr. Stevens' dissertation, which focuses on point defects in mid-infrared chalcopyrites, was based on research performed during this AFOSR project. He is remaining at West Virginia University as a postdoctoral fellow through the year 2000.

**DISSERTATIONS AND THESES:**

K. T. Stevens, Ph.D. Dissertation, "Electron-Nuclear Double Resonance Studies of Point Defects in $AgGaSe_2$ and $ZnGeP_2$," December 1999, West Virginia University. Adviser: L. E. Halliburton.

S. D. Setzler, Ph.D. Dissertation, "Electron Paramagnetic Resonance Studies of Electron and Hole Traps Related to Optical Damage in $KTiOPO_4$," March 1998, West Virginia University. Adviser: L. E. Halliburton.

E. Csomortani, M.S. Thesis, "A Computational and Experimental Study of $Fe^{3+}$ and $Cr^{3+}$ in $KTiOPO_4$," December 1997, West Virginia University. Adviser: L. E. Halliburton.

**PUBLICATIONS:**

1. "Electron Paramagnetic Resonance and Electron-Nuclear Double Resonance of $Ti^{3+}$ Centers in $KTiOPO_4$," S. D. Setzler, G. J. Edwards, K. T. Stevens, L. E. Halliburton, M. P. Scripsick, and N. C. Fernelius, submitted to Physical Review B.

2. "Electron Paramagnetic Resonance of Platinum Impurities in $KTiOPO_4$ Crystals," N. Y. Garces, K. T. Stevens, L. E. Halliburton, and D. Dawes, submitted to the Journal of Applied Physics.

3. "Photoluminescence and EPR of Phosphorus Vacancies in $ZnGeP_2$," M. Moldovan, K.

T. Stevens, L. E. Halliburton, P. G. Schunemann, T. M. Pollak, S. D. Setzler, and N. C. Giles, to appear in the Proceedings of the Materials Research Society (Fall 1999 Meeting).

4. "Temperature Dependent Hall Measurements Made on $CdGeAs_2$," A. J. Ptak, S. Jain, K. T. Stevens, T. H. Myers, P. G. Schunemann, S. D. Setzler, and T. M. Pollak, to appear in the Proceedings of the Materials Research Society (Fall 1999 Meeting).

5. "Photoinduced Changes in the Charge States of Native Donors and Acceptors in $ZnGeP_2$," K. T. Stevens, S. D. Setzler, P. G. Schunemann, T. M. Pollak, N. C. Giles, and L. E. Halliburton, to appear in the Proceedings of the Materials Research Society (Fall 1999 Meeting).

6. "Characterization of Defect-Related Optical Absorption in $ZnGeP_2$," S. D. Setzler, P. G. Schunemann, T. M. Pollak, M. C. Ohmer, J. T. Goldstein, F. K. Hopkins, K. T. Stevens, L. E. Halliburton, and N. C. Giles, Journal of Applied Physics 86, 6677 (1999).

7. "Electron Paramagnetic Resonance of a Cation Antisite Defect in $ZnGeP_2$," S. D. Setzler, N. C. Giles, L. E. Halliburton, P. G. Schunemann, and T. M. Pollak, Applied Physics Letters 74, 1218 (1999).

8. "Role of Silicon Impurities in the Trapping of Holes in $KTiOPO_4$ Crystals," K. T. Stevens, S. D. Setzler, L. E. Halliburton, M. P. Scripsick, and J. Rottenberg, Journal of Applied Physics 85, 1063 (1999).

9. "Native Defects in the Ternary Chalcopyrites," N. C. Giles and L. E. Halliburton, MRS Bulletin, Volume 23, No. 7, pp. 37-40, July, 1998.

10. "Electron-Nuclear Double Resonance Study of the Zinc Vacancy in Zinc Germanium Phosphide ($ZnGeP_2$)," K. T. Stevens, S. D. Setzler, L. E. Halliburton, N. C. Fernelius, P. G. Schunemann, and T. M. Pollak, Materials Research Society Symposium Proceedings, Volume 484, pp. 549-554 (1998).

11. "EPR and ENDOR Characterization of Nonlinear Optical Materials," L. E. Halliburton, in Critical Reviews of Optical Science and Technology, edited by R. A. Lessard and H. Franke, (SPIE, Bellingham, Washington), Vol. CR69, pp. 377-397, 1997.

12. "Electron Paramagnetic Resonance and Photoluminescence Studies of Point Defects in Zinc Germanium Phosphide ($ZnGeP_2$)," S. D. Setzler, L. E. Halliburton, N. C. Giles, P. G. Schunemann, and T. M. Pollak, Materials Research Society Symposium Proceedings, Volume 450, pp. 327-332 (1997).

**PRESENTATIONS:**

1. "Photoluminescence and EPR of Phosphorus Vacancies in $ZnGeP_2$," M. Moldovan, K. T. Stevens, L. E. Halliburton, P. G. Schunemann, T. M. Pollak, S. D. Setzler, and N. C. Giles, contributed poster, Materials Research Society 1999 Fall Meeting, Boston.

2. "Temperature Dependent Hall Measurements Made on $CdGeAs_2$," A. J. Ptak, S. Jain, K. T. Stevens, T. H. Myers, P. G. Schunemann, S. D. Setzler, and T. M. Pollak, contributed poster, Materials Research Society 1999 Fall Meeting, Boston.

3. "Photoinduced Changes in the Charge States of Native Donors and Acceptors in $ZnGeP_2$," K. T. Stevens, S. D. Setzler, P. G. Schunemann, T. M. Pollak, N. C. Giles, and L. E. Halliburton, 15-minute contributed talk, Materials Research Society 1999 Fall Meeting, Boston.

4. "Identification of Defects in $ZnGeP_2$ Using EPR and ENDOR," L. E. Halliburton and N. C. Giles, 30-minute invited talk, Nonlinear Optical Materials Workshop, Defence Evaluation and Research Agency (DERA), Malvern, United Kingdom, September 21, 1999.

5. "Defect Identification in $ZnGeP_2$ via EPR and ENDOR," L. E. Halliburton and N. C. Giles, one-hour presentation, Infrared Nonlinear Optical Semiconductor Workshop, Air Force Research Laboratory, Materials Directorate, Wright-Patterson AFB, Dayton, OH, August 26, 1999.

6. "Characterization of Native Donors and Acceptors in $ZnGeP_2$ Using EPR and ENDOR," L. E. Halliburton, one-hour invited seminar, Case Western Reserve University, Cleveland, OH, October 12, 1998.

7. "Role of Silicon Impurities in the Trapping of Holes in $KTiOPO_4$ Crystals," K. T. Stevens, S. D. Setzler, L. E. Halliburton, M. P. Scripsick, and J. Rottenberg, 15-minute contributed talk, Eastern Regional Conference on Crystal Growth and Epitaxy, American Association for Crystal Growth, Atlantic City, NJ, September 29, 1998.

8. "Characterization of Point Defects in $ZnGeP_2$ and KTP," L. E. Halliburton, 30-minute invited talk, Workshop on Nonlinear Optical Materials, Defence Evaluation and Research Agency (DERA), Malvern, United Kingdom, September 21 and 22, 1998.

9. "ENDOR Characterization of the Zinc Vacancy in Zinc Germanium Diphosphide," K. T. Stevens, S. D. Setzler, L. E. Halliburton, N. C. Fernelius, P. G. Schunemann, and T. M.

Pollak, 15-minute contributed poster, Materials Research Society 1997 Fall Meeting, Boston, MA, December 2, 1997.

10. "Current Status of Research on Nonlinear Optical Materials at West Virginia University," L. E. Halliburton, 30-minute invited talk, Air Force Nonlinear Optics Workshop, Fisk University, Nashville, TN, September 22, 1997. Organized by Mel Ohmer.

11. "EPR and ENDOR Characterization of Nonlinear Optical Materials," L. E. Halliburton, 45-minute invited talk, Annual Meeting of SPIE, The International Society for Optical Engineering, San Diego, CA, July 29, 1997.

12. "Electron Paramagnetic Resonance Studies of Point Defects in Zinc Germanium Phosphide ($ZnGeP_2$)," S. D. Setzler, L. E. Halliburton, N. C. Giles, P. G. Schunemann, and T. M. Pollak, 15-minute contributed talk, Materials Research Society 1996 Fall Meeting, Boston, MA, December 4, 1996.

13. "Defects Related to Gray Tracks in KTP," L. E. Halliburton, 30-minute invited talk, Annual Affiliates Meeting of the Center for Nonlinear Optical Materials, Stanford University, Palo Alto, CA, September 18, 1996.

## II. RESULTS OF POINT DEFECT STUDIES IN $ZnGeP_2$ AND $CdGeAs_2$ CRYSTALS

In recent years, considerable progress has been made in the growth of high-quality zinc germanium phosphide ($ZnGeP_2$) crystals for use in frequency conversion applications in the mid-infrared. A suitable birefringence, a large nonlinear optical coefficient, and good thermal conductivity make this material an excellent choice for optical parametric oscillators (OPOs) tunable in the 3 to 9 μm region. However, before $ZnGeP_2$ can achieve its full potential, a broad defect-related absorption band extending from 0.7 to 2.5 μm must be eliminated. This unwanted absorption band overlaps the desirable 2-μm pump region for mid-infrared OPOs and thus limits the maximum pump intensity that can be used in these devices. Several post-growth methods to reduce this absorption have been investigated, including lengthy thermal anneal, high-energy electron irradiation,[1] and gamma-ray irradiation.[2] These treatments, although helpful, have not eliminated the absorption problem in $ZnGeP_2$.

Nearly all of the $ZnGeP_2$ crystals described in the literature have been highly compensated, thus indicating nearly equal concentrations of donors and acceptors. There are two competing explanations for the nature of these donors and acceptors. One approach is

to assume these defects arise from disorder on the zinc and germanium sublattices, i.e., a zinc antisite defect would be an acceptor and a germanium antisite would be a donor. An alternate approach is to assume that the donors and acceptors are vacancy centers. Magnetic resonance techniques such as EPR, ENDOR, and ODMR make use of hyperfine interactions to identify specific defect models and thus can help to determine whether cation disorder or vacancies dominate in $ZnGeP_2$. Thus far, the zinc vacancy ( $V_{Zn}^-$ ), the phosphorus vacancy ( $V_P^0$ ), the germanium-on-zinc antisite ( $Ge_{Zn}^+$ ), and the phosphorus antisite ( $P_{Ge}^0$ ) have been detected by EPR.[3-6]

## A. EPR AND PL STUDIES

EPR shows the presence of two dominant native defects, a zinc vacancy and a phosphorus vacancy, in all of the $ZnGeP_2$ samples grown by the horizontal gradient freeze technique. The singly ionized zinc vacancy acceptor ( $V_{Zn}^-$ ) is paramagnetic (S = ½) and is easily seen without photoexcitation at temperatures below 50 K.[3] The unpaired spin is shared nearly equally by two phosphorus nuclei (I = ½, 100% abundant), which gives rise to triplets (1:2:1 line intensity ratios) in the EPR spectra. ENDOR has provided information about the lattice distortion surrounding this defect,[7] and has led to its assignment as $V_{Zn}^-$. This defect is present with slightly varying concentrations (on the order of $10^{18}$-$10^{20}$ $cm^{-3}$) in all samples studied.

Several additional intrinsic defects in $ZnGeP_2$ can be observed during photoexcitation. Laser excitation changes the valence of donors and acceptors, thus converting nonparamagnetic defects into paramagnetic forms. For example, phosphorus vacancies in $ZnGeP_2$ are present as singly ionized donors ( $V_P^+$ ), but it is their neutral state ( $V_P^0$ ) which is paramagnetic.[4] These latter centers are observed by illuminating the samples with above-band-gap (514.5 nm) or below-band-gap (632.8 nm) light at temperatures below 10 K. Even at these low temperatures, the neutral state is not stable and decays back to the singly ionized form in a matter of seconds or less. The EPR spectrum from the neutral phosphorus vacancy shows no hyperfine structure, indicating the unpaired spin does not strongly interact with phosphorus neighbors. This defect is usually observed at concentrations comparable to that of the zinc vacancies.

Another native paramagnetic defect, the phosphorus antisite, is not usually seen in $ZnGeP_2$ samples grown by the horizontal gradient freeze technique. However a recently grown sample did reveal a significant concentration of this donor. Kaufmann et al.[5] initially reported the presence of $P_{Ge}^0$ centers during photoexcitation at low temperatures.

The EPR spectrum of this center exhibits a large hyperfine splitting (about 750 G) with the central phosphorus nucleus and smaller ligand hyperfine interactions with the four nearest phosphorus neighbors. We can observe this spectrum at temperatures as high as 40 K, at which point the neutral charge state of the donor becomes unstable and converts back to its singly ionized form. This phosphorus antisite spectrum has only been present in one of the samples grown at Sanders, and for this reason it is not expected to play a major role in explaining the origin of the near-edge absorption in $ZnGeP_2$.

The optical absorption extending from 0.7 to 2.5 μm in $ZnGeP_2$ is commonly assumed to be due to point defects. Figure 1 shows this near-edge optical absorption from four different $ZnGeP_2$ samples. Also, EPR data from two of the samples are included in the figure. The EPR spectra shown are from singly ionized zinc vacancies ( $V_{Zn}^-$ ), and their relative intensities correlate well with the observed optical absorption. These results strongly suggest that the zinc vacancy acceptors play a direct role in the optical absorption phenomenon. Although not shown, large concentrations of phosphorus vacancy donors were also present in these samples. We conclude that the optical absorption is most likely due to several overlapping bands arising from an acceptor-to-donor transition and band-to-defect transitions. Support for this view comes from PL studies.

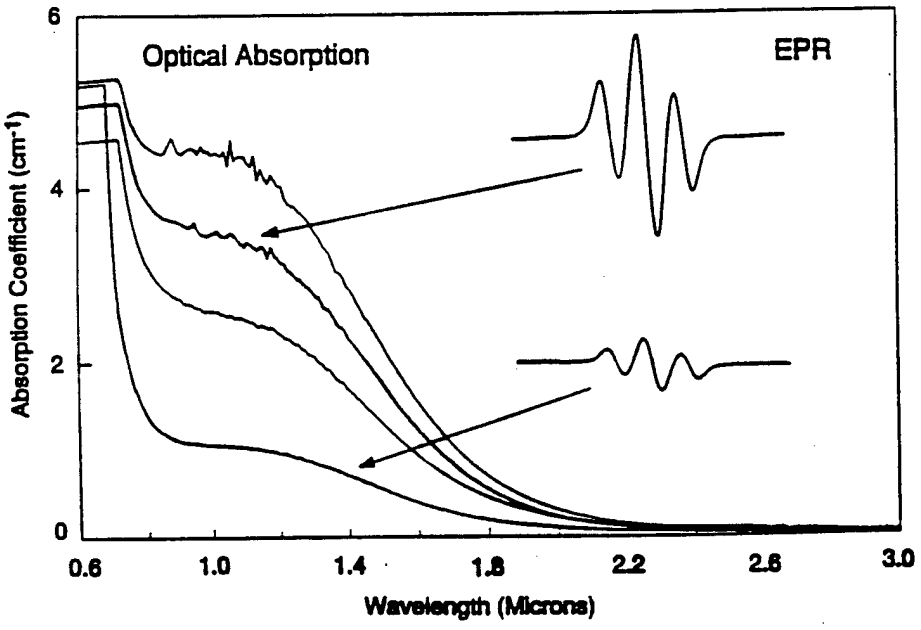


Figure 1. Correlation of near-edge optical absorption and zinc vacancy concentration as measured by EPR.

Results of photoluminescence experiments help to further connect these defects seen by EPR to the near infrared absorption. While PL spectra in $ZnGeP_2$ are often complex,[8] measurements taken on our samples indicate only two dominant emission bands at low temperature. Figure 2(a) shows PL spectra taken at 4.8 K with a polarizer placed parallel and perpendicular to the crystal c axis. These spectra have been corrected for the polarization response of the detection system. Subtracting one polarization from the other allowed us to decompose the spectrum into two overlapping bands. One band is partially polarized along the c axis of the crystal (the 1.42 eV band in Fig. 2(b)) and the other band is unpolarized (the 1.62 eV band in Fig. 2(c)). A possible explanation for the two bands is two distinct donor-acceptor-pair (DAP) recombinations. Such a model is not considered

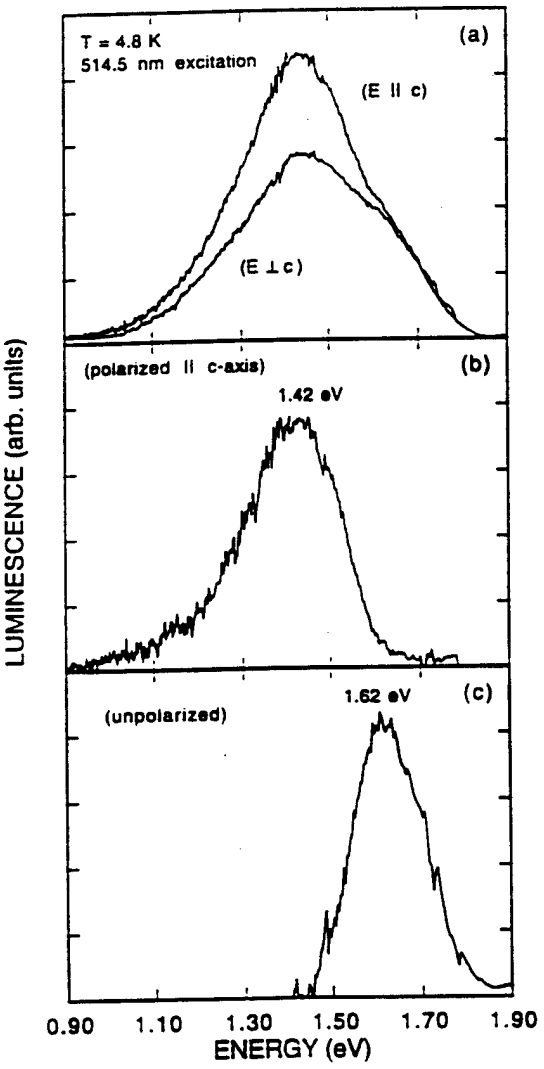


Figure 2. Photoluminescence of $ZnGeP_2$ measured at 4.8 K. (a) Spectra measured with emitted light polarized perpendicular and parallel to the crystal's c axis. These spectra are separated into a polarized part (b) and an unpolarized part (c).

likely since EPR data, thus far, have revealed the existence of only one dominant donor ($V_P^0$) and one dominant acceptor ($V_{Zn}^-$) in our samples. It is more likely that one of the observed bands is DAP (i.e., the 1.42-eV band) and the other is a band-to-impurity transition, i.e., an (e,A) or (D,h) transition. Since the PL spectra shown in Fig. 2(a) are also observed with below-band-gap light (632.8 nm), we suggest that the 1.62-eV emission is donor-hole (D,h) recombination. We find that the emission and optical absorption exhibit the same polarization behavior and, furthermore, our PL polarization study is at variance with the report of McCrae et al.[9]

From our EPR and PL results, we construct an energy-level diagram in Fig. 3 using a single-donor/single-acceptor model where $V_{Zn}^-$ and $V_P^+$ are the dominant acceptor and donor defects. We have earlier suggested that a significant DAP emission occurs near 1.4 eV at liquid-helium temperature, and this is illustrated in the figure. Donor-hole transitions, previously assigned to an emission near 1.6 eV, are also illustrated in the figure. The optical absorption, which limits device performance, peaks near 1 μm (1.2 eV) at room temperature, as shown in Fig. 1. A portion of this optical absorption can be attributed to the transitions from the acceptors to the donors. The room temperature absorption and the low temperature emission peaks do not directly coincide, but this is explained in large part by a ~0.1 eV change in band gap with temperature. Additional transitions from the valence band to the donors and from acceptors to the conduction band may be contributing to the high-energy side of the observed broad optical absorption. Likewise, transitions from valence band states to neutral acceptors may give rise to absorption in the region beyond 2 μm.

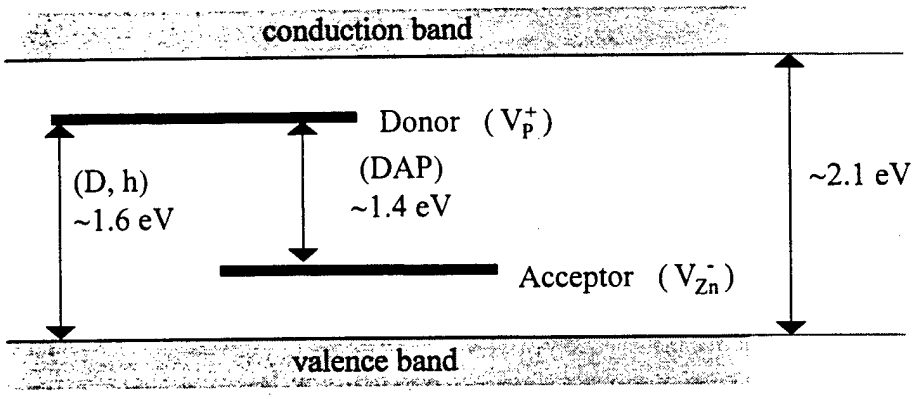


Figure 3. Energy-level diagram based on two dominant native defects.

A preliminary investigation of the time-decay behavior of the PL bands has been completed. Figure 4 shows the data obtained by monitoring the DAP emission at 1.42 eV after an 8-ns, 532-nm excitation pulse. Because of the low intensity of the emitted light, 1000 decays were accumulated. The decay occurs over a time window extending out to approximately 20 μs and can not be fit by a single exponential. These results support our previous assignment of this emission of DAP recombination in an indirect-gap semiconductor. We also measured the decay of the PL occurring at 1.62 eV and found a similar dependence on time.

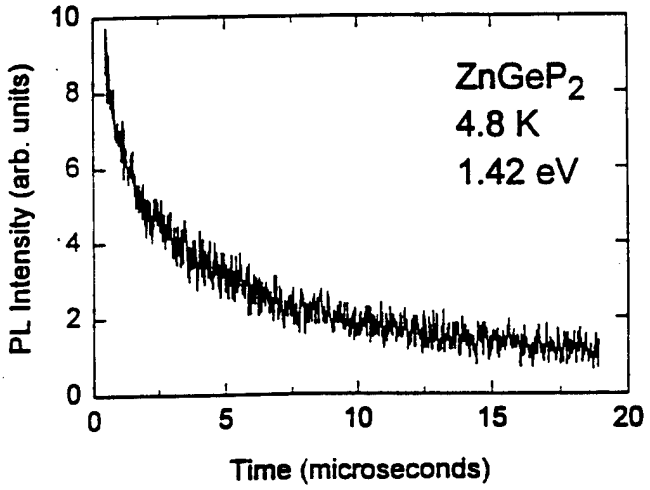


Figure 4. Time decay of the DAP emission at 1.42 eV.

EPR, ENDOR, PL, and time-resolved PL are well suited to study defects in $ZnGeP_2$. Their usefulness, however, is not restricted to studying native defects. Substitutional manganese was reported by Baran et al.,[10] and we have recently "rediscovered" this defect in material grown by the horizontal gradient freeze technique. A careful analysis of the $Mn^{2+}$ EPR spectrum, shown in Fig. 5, yields spin-Hamiltonian parameters similar to

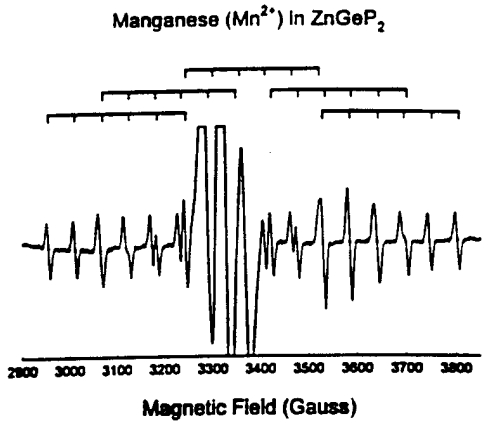


Figure 5. EPR spectrum of $Mn^{2+}$ in $ZnGeP_2$.

those reported by Baran, et al. The defect is an S = 5/2 system interacting with an I = 5/2 nucleus (100% abundant). A small crystal field, due to the crystal's tetragonal symmetry, splits the spectrum into five sets of six lines. The three larger lines in the center of the spectrum in Fig. 5 are due to the zinc vacancy. The only sample this manganese spectrum has been seen in was the one in which the antisite $P_{Ge}^{0}$ was also observed. This piece was cut from the end of a boule, indicating a possible variation in stoichiometry, and photoluminescence studies have not yet been performed on this sample.

## B. ENDOR FROM THE ZINC VACANCY IN $ZnGeP_2$

The dominant singly ionized acceptor in $ZnGeP_2$ is paramagnetic (S = ½) and is easily seen without photoexcitation at temperatures below 50 K.[3] Its *c*-axis EPR spectrum is shown in Fig. 6. The unpaired spin is shared equally by two phosphorus nuclei (I = 1/2, 100% abundant), and this gives rise to triplets (1:2:1 line intensity ratios) in the EPR spectra. As previously described by Rakowsky et al.,[3] the angular dependence of the EPR spectrum can be explained in terms of four crystallographically equivalent orientations of the defect. One of these sites is illustrated on the left in Fig. 7, where the two phosphorus ions labeled $P_A$ are central to the defect. The principal values of the g matrix are 2.002, 2.021, and 2.074 and the corresponding principal axes for the particular site in Fig. 7 are the [011], [$\bar{1}$00], and [0$\bar{1}$1] directions, respectively.[3]

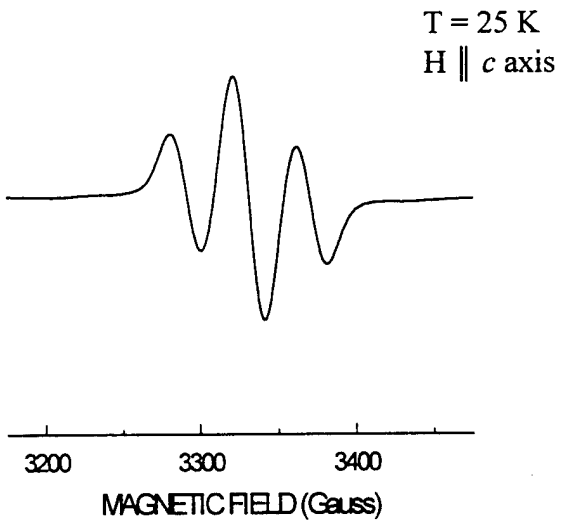


Figure 6. EPR spectrum of the dominant acceptor in $ZnGeP_2$.

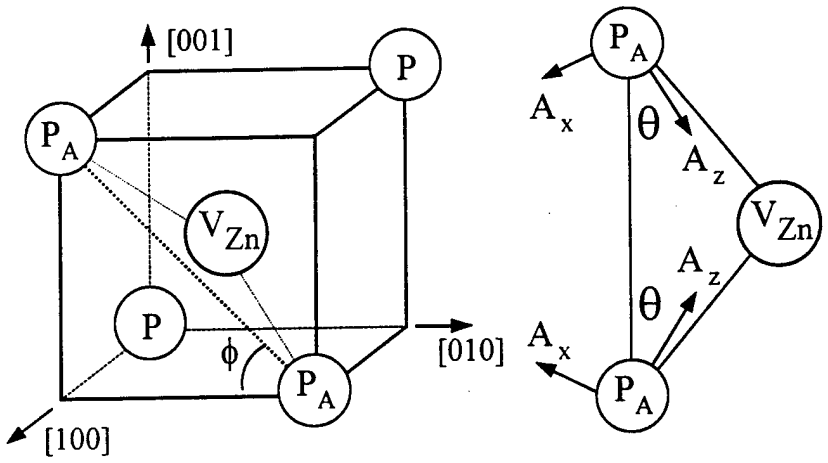


Figure 7. Zinc-vacancy model for the dominant acceptor in $ZnGeP_2$. The $P_A$ phosphorus ions sharing the unpaired spin are shown on the left. The hyperfine principal axes for these two nuclei are on the right.

An ENDOR study of the resolved hyperfine interactions (i.e., with the two primary phosphorus nuclei) has been previously reported by our laboratory.[7] This work revealed that the acceptor has significant lattice distortion, and it was argued that this provided strong evidence in favor of the zinc-vacancy model for the dominant acceptor in $ZnGeP_2$. In Fig. 7, the parameter $\phi$ represents the angle between the interphosphorus axis (heavy dashed line) and the basal plane of the crystal, i.e., the (001) plane. The initial ENDOR analysis[7] gave a value of 37.8° for this angle, which is considerably different from the value of 44.5° for the undistorted lattice. Such a large lattice distortion would not be expected for a $Zn_{Ge}$ center because of its regular tetrahedral bonding.

It was recently suggested,[11] and it now has been verified in the present investigation, that the sample was slightly out of the *c-a* plane when the ENDOR angular data reported in Figure 3 of Reference 7 was taken. An analysis of in-plane ENDOR data (both from the *c-a* plane and the *a-a* plane) shows that the two EPR-resolved phosphorus hyperfine interactions, are equivalent, within experimental error. Our previous study had concluded that the unique principal values ($A_{1,z}$ and $A_{2,z}$) for these two primary phosphorus interactions differed by about 2.4%. The revised values for the spin-Hamiltonian parameters are given in Table I. These more recent results do not affect the earlier arguments made in favor of the zinc-vacancy model, however, since the parameter $\phi$ changes only slightly from 37.8° to 37.9°.

In the present project, we have extended the ENDOR technique to study additional phosphorus hyperfine interactions not resolved in the EPR spectra. These weaker interactions have ENDOR lines below 20 MHz, while the stronger hyperfine from the primary $P_A$ pair of phosphorus nuclei had ENDOR lines between 40 and 75 MHz. Figure 8 shows the lower frequency ENDOR spectrum when the magnetic field is parallel to the *c* axis. This

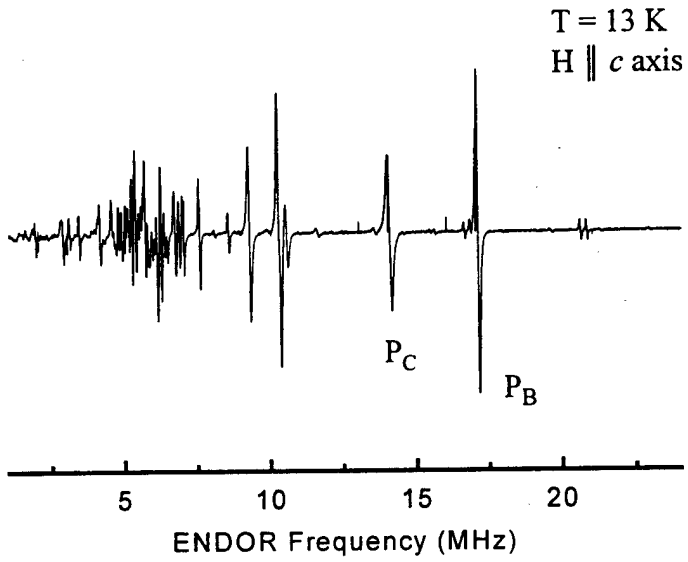


Figure 8. Low-frequency ENDOR spectrum for the acceptor.

spectrum contains many lines, which indicates that the wave function for the acceptor overlaps a large number of neighboring nuclei. In the remainder of this section, attention is focused on the two lines located near 17 MHz and 14 MHz in Fig. 8. For convenience, they are labeled the $P_B$ pair and the $P_C$ pair of phosphorus nuclei, respectively. Because each of these ENDOR lines has a sufficiently large hyperfine parameter A, they and their companion lines are separated by $2\nu_N$ and centered on A/2. In our ENDOR experiments, the free nuclear-resonance frequency for phosphorus ($\nu_N$) was approximately 5.74 MHz. This places the two companion lines near 2.5 MHz and 5.5 MHz, but these are regions where the spectrometer has less sensitivity and where large numbers of ENDOR lines overlap. Lower frequency companion lines have been observed for the 17 and 14 MHz lines when the magnetic field is parallel to the *c* axis, thus demonstrating that the responsible nuclei are phosphorus, but it proved impossible to follow the angular dependence of these low-frequency companions. The angular dependences of the 17 MHz and the 14

MHz ENDOR lines were easy to follow, however. Figure 9 shows the observed angular variation associated with the 17 MHz interaction ($P_B$ pair) as the magnetic field is rotated

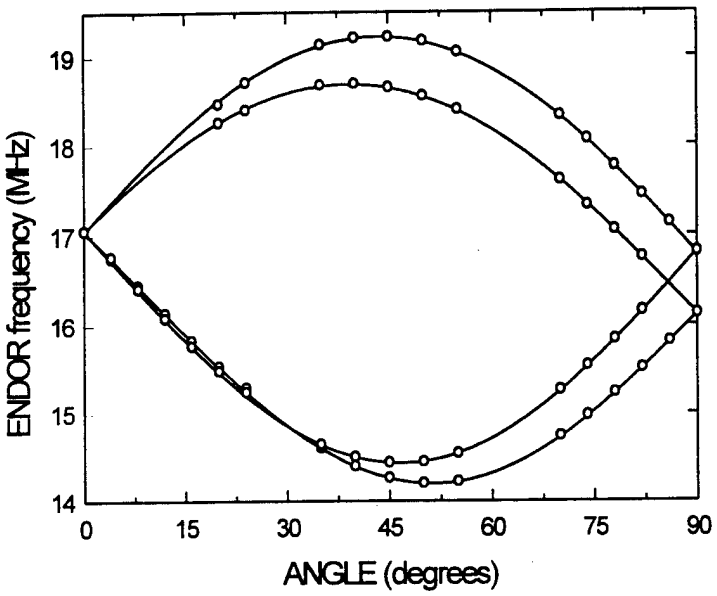


Figure 9. Angular dependence of the ENDOR spectrum for the $P_B$ pair of phosphorus nuclei. Data points are experimental while the solid lines are calculated using the parameters in Table I. Rotation is from the *c* axis (0°) to the *a* axis (90°).

from the *c* axis to the *a* axis. Similar angular data is shown in Fig. 10 for the 14 MHz interaction ($P_C$ pair). Data for both interactions also were taken with the magnetic field along the [110] direction.

The experimental data in Figs. 9 and 10 have been fit to the following spin-Hamiltonian with S = 1/2 and I = 1/2.

$$H = \beta \mathbf{S} \cdot \mathbf{g} \cdot \mathbf{B} + \mathbf{S} \cdot \mathbf{A} \cdot \mathbf{I} - g_N \beta_N \mathbf{B} \cdot \mathbf{I} \qquad (1)$$

The first term is the electron Zeeman, the second term is the hyperfine interaction with one phosphorus, and the third term is the phosphorus nuclear Zeeman. Values for the g matrix were taken from Reference 3. A least-squares fitting program repeatedly diagonalized the 4 x 4 Hamiltonian matrix to obtain the set of parameters which best fit the experimental data. These results are presented in Table I. Five parameters were included in the fitting procedure for each of the two pairs of phosphorus nuclei. Figure 11 shows the location of

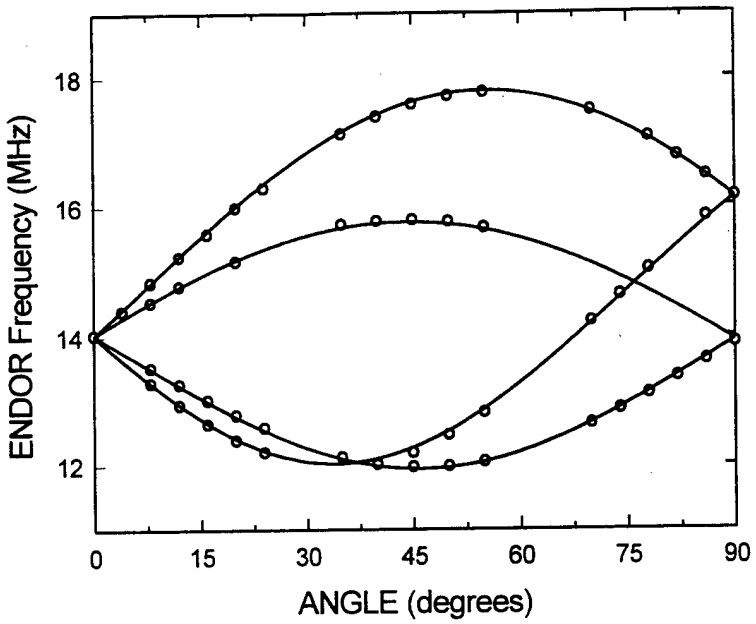


Figure 10. Angular dependence of the ENDOR spectrum for the $P_C$ pair of phosphorus nuclei. Closed circles are experimental while the solid lines are calculated using the parameters in Table I. Rotation is from the *c* axis (0°) to the *a* axis (90°).

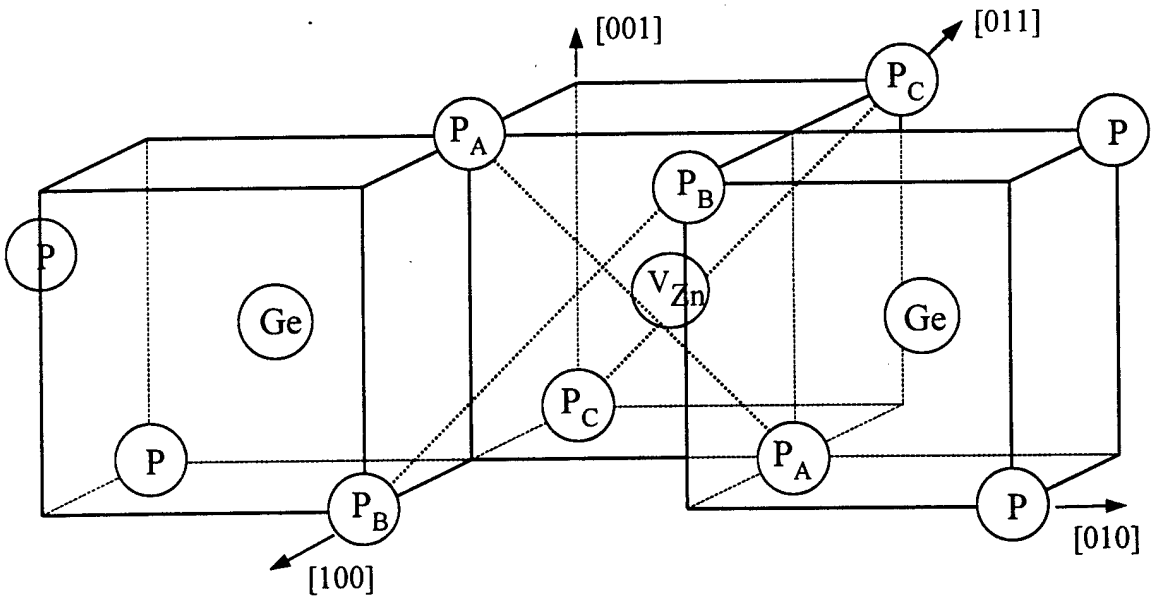


Figure 11. Zinc-vacancy model for the dominant acceptor in $ZnGeP_2$ showing the $P_A$, $P_B$, and $P_C$ pairs of phosphorus nuclei. The zinc vacancy is in the rear center "cube," while the left and right front "cubes" have germanium ions at their centers.

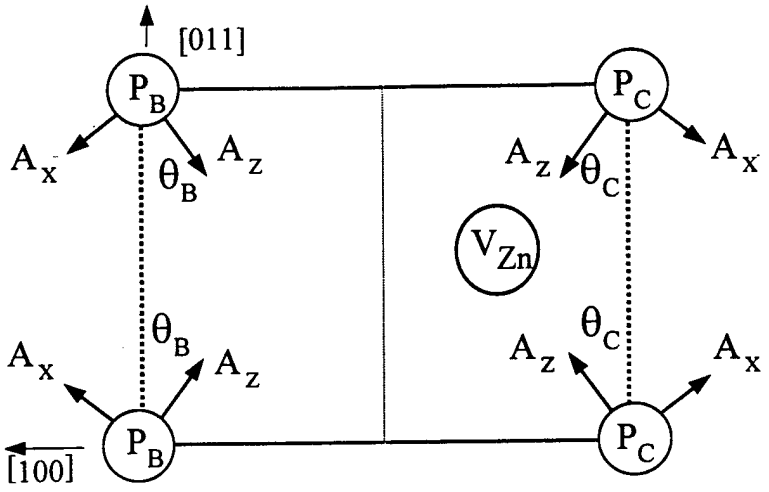


Figure 12. Hyperfine principal axes directions for the $P_B$ and $P_C$ pairs of phosphorus nuclei.

the phosphorus ions we have assigned to the $P_B$ and $P_C$ pairs. There are three connected "cubes" illustrated in Fig. 11; the left and right "cubes" in the front are $GeP_4$ units while the back "cube" in the center contains the zinc vacancy. The $P_A$ pair is located between the $P_B$ and $P_C$ pairs. The $P_A$ and $P_C$ pairs are adjacent to the zinc vacancy, but on opposite sides. The $P_B$ pair is not adjacent to the vacancy. Figure 12 represents the $(01\bar{1})$ plane, containing the $P_B$ and $P_C$ pairs of phosphorus nuclei, and describes the principal axes directions. We have assigned the $P_C$ pair of phosphorus to be adjacent to the vacancy because they appear to have significant lattice distortion (a value of 34.3° for $\phi$ compared to 44.5° for the unperturbed lattice). This is similar to the result for the $P_A$ pair and is expected for all nuclei neighboring the vacancy. In contrast, the value of $\phi$ for the remaining pair is 46.6°, which suggests only a small amount of lattice distortion. Thus, the $P_B$ pair is assigned to nuclei away from the vacancy.

The zinc-vacancy model continues to be the most likely choice for the dominant acceptor in $ZnGeP_2$. ENDOR results have been obtained from a second and third pair of phosphorus nuclei (labeled $P_B$ and $P_C$ pairs) whose hyperfine is not resolved in the EPR spectra. The $P_C$ pair shows significant lattice distortion and the $P_B$ pair does not, although they have similar hyperfine interactions with the unpaired spin, i.e., their principal values are comparable. This is understandable if the $P_C$ pair is adjacent to the zinc vacancy and

the $P_B$ pair is more distant from the vacancy, e.g., part of the neighboring $GeP_4$ units. It is difficult to obtain absolute evidence on which to assign the acceptor to a specific model, but thus far the singly ionized zinc vacancy ($V_{Zn}^-$) is consistent with all data. Future studies must characterize the remaining weak phosphorus ENDOR lines and search for possible zinc and germanium ENDOR lines.

Table I. Spin-Hamiltonian parameters. Values are presented for the primary ($P_A$ pair) and the first ($P_B$ pair) and second ($P_C$ pair) weak phosphorus hyperfine interactions. The angle $\phi$ is measured from the internuclear axis to the basal plane and the angle $\theta$ is defined in Figs. 7 and 12.

| Nuclei | $A_x$ (MHz) | $A_y$ (MHz) | $A_z$ (MHz) | $\theta$ | $\phi$ |
|---|---|---|---|---|---|
| $P_A$ pair | 95.5 | 99.3 | 143.5 | 31.4° | 37.9° |
| $P_B$ pair | 16.9 | 17.5 | 30.0 | 30.7° | 46.6° |
| $P_C$ pair | 12.3 | 12.6 | 27.0 | 28.6° | 34.3° |

## C. CHARACTERIZATION OF A CATION ANTISITE DEFECT IN $ZnGeP_2$

The observation[3,4] of high concentrations ($10^{18}$ to $10^{20}$ $cm^{-3}$) of $V_{Zn}^-$ centers and $V_P^0$ centers in many $ZnGeP_2$ crystals supports the nonstoichiometric vacancy-based scheme for acceptors and donors. The alternative cation disorder scheme involving large concentrations of antisite $Ge_{Zn}$ donors and $Zn_{Ge}$ acceptors has, thus far, not been directly supported by experiment. In principle, however, both vacancies and cation antisite defects can coexist in $ZnGeP_2$ crystals, and we expect that specific growth conditions may increase the possibility of forming a subset of the antisite defects. In the present section, we describe a photoinduced EPR spectrum from a new donor in $ZnGeP_2$ and suggest that the most likely model for this defect is a germanium ion on a zinc site. We observed this defect in all of the crystals available to us, and its concentration was usually about 10% of the singly ionized zinc vacancy concentration.

The $ZnGeP_2$ crystals used in this study were grown at Sanders (a Lockheed Martin Company) by the horizontal-gradient freeze technique.[12] After growth, these crystals were thermally annealed at 550°C for 300 hours while surrounded by $ZnP_2$ powder. This thermal treatment reduces the unwanted optical absorption peaking near 1 μm. Dimensions of the EPR samples were approximately 5 x 3 x 2 $mm^3$ along the [100], [010], and [001] di-

rections, respectively. A Bruker ESP 300 spectrometer operating at 9.45 GHz was used to obtain the EPR data. An Oxford Instruments ESR-900 helium gas flow system maintained the sample temperature at selected values between 8 and 50 K. Slots in the end of the $TE_{102}$ microwave cavity provided optical access to the sample. The photoexcitation source was a helium-neon laser (632.8 nm) operating cw with a power of 5 mW incident on the cavity. This excitation wavelength is slightly below the band edge of $ZnGeP_2$, which is near 600 nm at liquid helium temperatures.

A dominant paramagnetic acceptor is present in all of our $ZnGeP_2$ crystals. Its EPR spectrum is shown in Fig. 13(a), where the data were taken at 35 K in the "light-off" condition with the magnetic field parallel to the c axis. For this orientation of magnetic field, the spectrum consists of a triplet of lines (1:2:1 intensity ratio) due to hyperfine interactions with two equivalent phosphorus nuclei. The separation between adjacent lines is approximately 40 gauss. It has been previously suggested that the model[3,7,13] for this defect is a singly ionized zinc vacancy, i.e., a $V_{Zn}^{-}$ acceptor.

Illuminating the $ZnGeP_2$ crystals with laser light while at temperatures below 50 K introduces a new EPR spectrum. The outer portions of this photoinduced spectrum appear in the low and high field regions of Fig. 13(b). The central portion of the new spectrum, however, can not be directly observed because of interference from the $V_{Zn}^{-}$ acceptor (described in the preceding paragraph). The data in Fig. 13(b) were taken at 35 K in the "light-on" condition with the magnetic field parallel to the c axis. The dominating triplet set of lines from the $V_{Zn}^{-}$ center has increased in intensity when the crystal was exposed to the laser light, as illustrated in Fig. 13(b), and we attribute this increase to the temporary conversion of doubly ionized zinc vacancies ($V_{Zn}^{--}$ centers) to the singly ionized state ($V_{Zn}^{-}$ centers). An alternative explanation, which we consider to be less likely for this increase of $V_{Zn}^{-}$ centers, is the temporary conversion of neutral zinc vacancies ($V_{Zn}^{0}$ centers) to the singly ionized state ($V_{Zn}^{-}$ centers) as a result of optically pumping electrons from a shallower ionized acceptor. It was possible to obtain a complete view of the new photoinduced EPR spectrum by generating a "difference" spectrum, i.e., by first adjusting the intensity of the $V_{Zn}^{-}$ signal in Fig. 13(a) to be equal to the intensity of the $V_{Zn}^{-}$ signal in Fig. 13(b) and then subtracting the adjusted "light off" spectrum from the "light on" spectrum. The resulting spectrum is shown in Fig. 13(c). The signal from the $V_{Zn}^{-}$ acceptor has been effectively eliminated and the new photoinduced EPR spectrum is shown in its entirety. A small photoinduced signal near 3250 G in Fig. 13(c) is due to neutral phosphorus vacancies.[4] The number of phosphorus vacancies in this sample is similar (within a factor of three) to the number of zinc vacancies, but the signal from the $V_{P}^{0}$ centers is

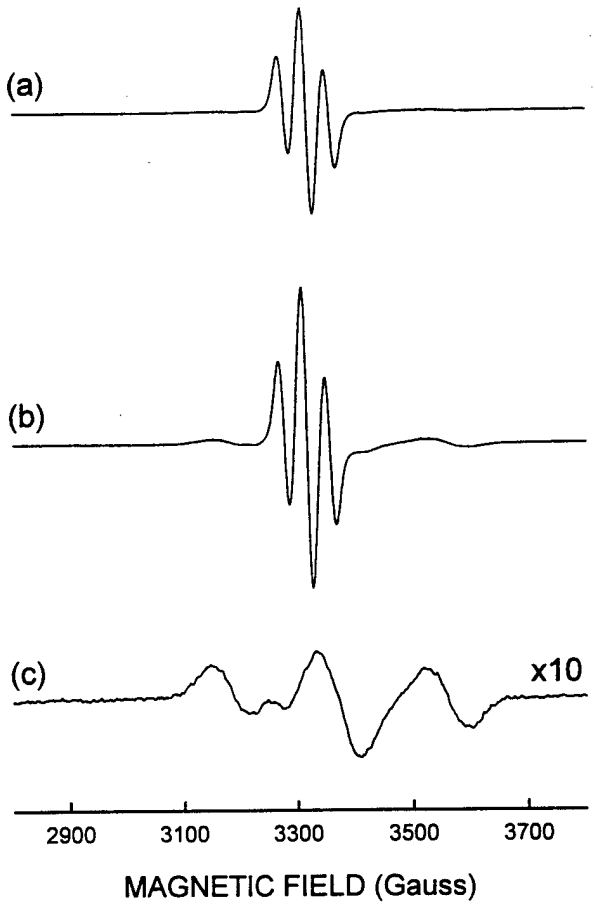


Figure 13. EPR spectra from $ZnGeP_2$ taken at 35 K with the magnetic field parallel to the c axis. Trace (a) is the "light-off" spectrum and trace (b) is the "light-on" spectrum. The spectrometer settings were the same for traces (a) and (b). Trace (c) shows a underlying widely split EPR signal, multiplied by a factor of 10, after the sharper central three-line spectrum has been removed by subtracting a "normalized" trace (a) from trace (b).

small in Fig. 13(c) because of the short lifetime of these neutral centers at 35 K (i.e., they decay at a sufficiently fast rate that the low-power excitation laser cannot establish a large steady-state concentration). The $V_P^0$ centers are best observed at temperatures below 10 K, where their lifetimes are significantly longer.

The new photoinduced spectrum consists of a triplet set of lines (1:2:1 intensity ratio) with an isotropic g value of 2.0026. Adjacent components of the spectrum are split by 189 G when the magnetic field is parallel to the c axis. This splitting changes to 179 G

when the magnetic field is parallel to the a axis of the crystal. A reasonable explanation for the triplet pattern in this new EPR spectrum is equivalent (or nearly equivalent) hyperfine interactions with two $^{31}P$ nuclei (I = 1/2, 100% abundant). The appropriate S = 1/2 spin-Hamiltonian is then

$$\begin{aligned} H = {} & g\beta(S_xB_x + S_yB_y + S_zB_z) \\ & + A_{\parallel}S_zI_{1z} + A_{\perp}(S_xI_{1x} + S_yI_{1y}) \\ & + A_{\parallel}S_zI_{2z} + A_{\perp}(S_xI_{2x} + S_yI_{2y}) \end{aligned} \qquad (2)$$

where $A_{\parallel}$ = 189 G and $A_{\perp}$ = 179 G. These hyperfine parameters can be rewritten in terms of an isotropic parameter a and an anisotropic parameter b by using $A_{\parallel}$ = a - 2b and $A_{\perp}$ = a +b. This gives a = 182 G and b = 3.3 G. The width of the individual lines in the spectrum is approximately 70 G and does not vary with magnetic field direction. We found that the EPR spectrum is best observed when the sample temperature is near 35 K and the excitation wavelength is close to the band edge. The 632.8-nm wavelength of the helium-neon laser worked well as an excitation source, while a cw 1064-nm Nd:YAG laser (100 mW) produced only a barely observable EPR spectrum. At 35 K, removing the exciting light from the sample caused the spectrum to decay to an unobservable concentration in about 10 minutes.

We now turn to a discussion of the identity of the defect responsible for the new photoinduced EPR spectrum in $ZnGeP_2$. A lack of significant angular dependence in this tetragonal-symmetry lattice argues against a transition-metal-ion assignment. Thus attention is focused on native defects. In general, there are three vacancy and six antisite candidates, if interstitials and complexes of defects are not considered. The observation of resolved hyperfine from two nearly equivalent phosphorus ions strongly suggests that the defect is centered on a cation site. This restricts our consideration to the two cation vacancies ($V_{Zn}$ and $V_{Ge}$) and the two cation antisites ($Ge_{Zn}$ and $Zn_{Ge}$). The zinc vacancy has already been assigned to another EPR spectrum,[3,7,13] and germanium vacancies are unlikely since our $ZnGeP_2$ crystals are believed to have excess germanium. [Note: This excess of germanium results from the higher volatility of zinc and phosphorus during crystal growth.] The zinc-on-a-germanium center ($Zn_{Ge}$) also would be less likely in a germanium-rich environment. This leads us to conclude that the germanium-on-a-zinc center ($Ge_{Zn}$) is the most likely candidate for the new photoinduced EPR spectrum.

The $Ge_{Zn}$ defect is a donor and is paramagnetic (S = 1/2) in its singly ionized state, i.e., a $Ge_{Zn}^{+}$ center. This antisite defect is doubly ionized (a $Ge_{Zn}^{++}$ center) in the "light-off" condition and is converted to the singly ionized state in the "light-on" condition.

We have suggested earlier in this section that doubly ionized zinc vacancies ( $V_{Zn}^{--}$ centers) are the source of the electrons which transiently convert the doubly ionized antisite center to its singly ionized state. This is illustrated in Fig. 13, where the intensity of the central three-line EPR spectrum (assigned to the $V_{Zn}^{-}$ centers) was found to increase during illumination. Using the data in Fig. 13, a comparison of spin concentrations shows that the number of $Ge_{Zn}^{+}$ centers formed by the light in Fig. 13(b) is equal (within experimental error) to the number of additional $V_{Zn}^{-}$ centers formed by the light. On the basis of these data, we suggest that the concentration of germanium-on-zinc antisite defects is approximately 30 to 33% of the concentration of zinc-vacancy defects in this particular $ZnGeP_2$ sample. We note that this sample had the largest $Ge_{Zn}^{+}$ EPR signal of any $ZnGeP_2$ crystals we examined, while the more typical situation was to have a concentration of germanium-on-zinc antisite defects which was approximately 10% of the concentration of zinc-vacancy centers.

A simple analysis of the phosphorus hyperfine parameters for the $Ge_{Zn}^{+}$ center suggests that approximately 15% of the unpaired spin is on the two primary phosphorus ions. This value was obtained by comparing our experimental hyperfine results (a = 182 G and b = 3.3 G) to theoretical estimates (a = 3977 G and b = 111 G) corresponding to the unpaired spin being in either a valence s or p orbital at a phosphorus free atom.[14] We recognize that our experimental value for b is inexact, since a detailed angular dependence of the EPR signal was not acquired, and the 15% value quoted may change slightly as more data become available. Nevertheless, it is clear that the majority of the unpaired spin is localized on ions other than the two primary phosphorus. Our proposed model is consistent with this observation since it would place much of the unpaired spin on the central germanium ion. Detection of resolved hyperfine lines from the $^{73}Ge$ nucleus (I = 9/2, 7.8% abundant) is not expected because of the 70-G linewidth of the EPR signal and the isotope's low abundance.

In conclusion, we have observed a new photoinduced EPR spectrum in $ZnGeP_2$. Two factors, a significant hyperfine interaction with two adjacent phosphorus nuclei and the germanium-rich nature of our $ZnGeP_2$ crystals, lead us to assign the new spectrum to the singly ionized state of the germanium-on-a-zinc antisite (i.e., the $Ge_{Zn}^{+}$ center). The $Ge_{Zn}^{+}$ centers are temporarily formed when an electron is transferred from $V_{Zn}^{--}$ centers to $Ge_{Zn}^{++}$ centers. We note that this is the first report of EPR from cation antisite defects in $ZnGeP_2$. Additional studies, including electron-nuclear double resonance (ENDOR) experiments, are needed to further verify the assignment made in the present study.

## D. HALL MEASUREMENTS ON $CdGeAs_2$

$CdGeAs_2$ has attracted much attention in recent years for its potential as a frequency conversion material operating in the infrared. It has the highest nonlinear optical coefficient of any known phase-matchable compound (236 pm/V). $CdGeAs_2$ has shown promise for the second harmonic generation of a $CO_2$ laser to produce a tunable infrared source for the mid-infrared wavelengths[15] which are potentially useful for the monitoring of many atmospheric pollutants. Unfortunately, this material has suffered from several problems that have limited its usefulness, although some success has been achieved.[15,16] These drawbacks include a high background of p-type carriers from native acceptors and residual impurities, and a large anisotropy in the coefficient of thermal expansion. This latter property has made it very difficult to grow large, crack-free crystals.

A range of acceptor activation energies have been reported for $CdGeAs_2$. Fischer et al.[17] have reported values for $E_a$ ranging between 100 and 150 meV in undoped material. Bairamov et al.[18] have studied both undoped as well as Cu- and Ga-doped material. In their study, undoped samples indicated an intrinsic, or native, defect possibly related to cadmium vacancies with an acceptor level around 150 to160 meV. The Cu and Ga produced acceptor levels about 120 to 130 meV above the valence band. The present study indicates that both native levels and extrinsic impurities continue to play an important role in $CdGeAs_2$.

The $CdGeAs_2$ samples studied at West Virginia University were grown at Sanders, A Lockheed Martin Company (Nashua, NH). Both intentionally and unintentionally doped samples were included in the study. Two different growth methods were employed, horizontal gradient freeze (HGF) and travelling heater method (THM). Both techniques produced similar material. Temperature dependent Hall effect measurements were performed at West Virginia University using a system similar to the typical Keithley Instruments Hall effect set-up. Indium contacts were soldered to the samples in the standard Van der Pauw geometry.

Since $CdGeAs_2$ is a highly anisotropic crystal, specially matched sets of samples were fabricated from each boule for Hall analysis. Hall measurements performed on the sample that had the c-axis perpendicular to the plane of the sample ($c_\perp$) allowed measurement of the carrier concentration, the mobility, and the resistivity along the a-axis. The other sample had the c-axis in the plane of the sample, parallel to one edge ($c_\parallel$), allowing the resistivity of both the a- and c-axes to be determined directly. For each matched set, the a-axis resistivities agreed reasonably well, with the worse case differing by a factor of

two. It is reasonable to assume this variation is due primarily to carrier concentration variations within a boule, and thus the resistivity ratio coupled with the a-axis mobility determines the c-axis mobility, giving a complete set of electrical properties for each direction in the crystal. In addition to the electrical data, infrared absorption measurements were performed at room temperature from 2-20 μm using a Nicolet Magna-IR 550 FTIR spectrometer.

Representative data from the temperature dependent Hall measurements made on the $c_\perp$ samples of $CdGeAs_2$ are plotted in Figure 14. Hall effect measurements of this type indicated p-type material in all but one case. Shown in Figure 14 are the carrier concentration and mobility measured for sample 49. The room temperature carrier concentration for this particular sample was ~$1 \times 10^{15}$ $cm^{-3}$ with the effect of carrier "freeze-out" easily seen. The maximum hole mobility was seen to be ~225 $cm^2$/V-sec occurring ~190 K. Also of note, the Hall coefficient changes signs, from positive to negative, at about 350 K, indicating that intrinsic carrier concentration effects are becoming important near this temperature. The activation energy of the acceptors can be determined from the low-temperature carrier concentration data, where the intrinsic electrons have not yet become important.

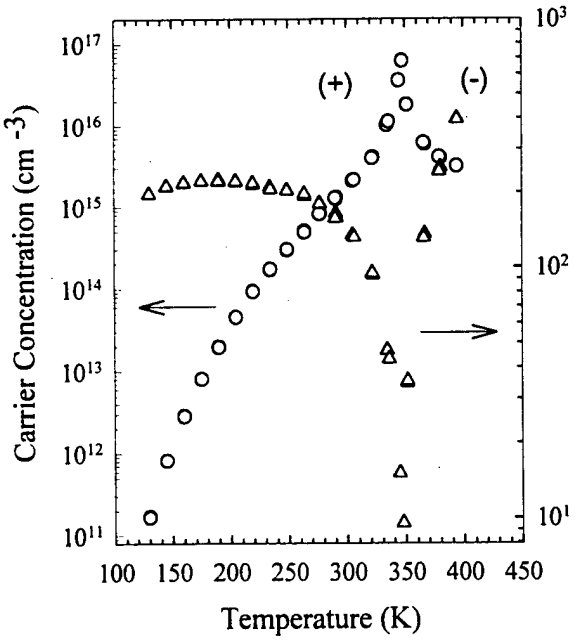


Figure 14. Typical electrical properties of cadmium germanium arsenide.

The data were fit to the full charge balance equation, based on one acceptor level and a fully ionized shallow donor with no assumptions about the relative concentrations of impurities.[19] Due to the large activation energy of the acceptors, complete ionization would only occur at temperatures where conduction is dominated by intrinsic electrons. With the constraint of incomplete ionization, the fitting procedure could only determine the compensation of the material, i.e. the ratio of the number of donors to the number of acceptors. Table II contains information on all of the samples that were measured, including the compensation ratio and the activation energy of the acceptors.

**Table II. Hall measurement results on selected $CdGeAs_2$ samples.**

| Sample | Dopant | RT Carrier Concentration ($10^{16}$ cm$^{-3}$) | Activation Energy (meV) | Compen-sation Ratio | p-to-n Transition Temp. (K) | RT Absorption Coefficient at 5.75μm (cm$^{-1}$) |
|---|---|---|---|---|---|---|
| 29 | Cr | 0.21 | 141 | 0.71 | 377 | 1.1 |
| 30 | Ag | 0.20 | 131 | 0.77 | 417 | 1.9 |
| 31 | Undoped | 1.8 | 110 | 0.26 | -- | 11.0 |
| 34 | Se | -8.8 | <20 | -- | -- | 0.9 |
| 37 "dark" | Undoped | 3.1 | 109 | 0.25 | -- | 18.4 |
| 37 "light" | Undoped | 0.089 | 125 | 0.95 | 329 | 1.8 |
| 49 | Se | 0.12 | 154 | 0.69 | 346 | 1.3 |
| 50 | Undoped | (a) | 153 | 0.83 | 259 | 3.5 |
| 51 | Te | 0.2 | 164 | 0.50 | 336 | 0.4 |

(a) Not reliable due to proximity to Hall coefficient transition

If the extrinsic p-type doping is sufficiently low, or the sample is highly compensated, intrinsic conduction effects become important. Ambipolar conduction effects can result in the Hall coefficient changing from positive to negative since the electron mobility in $CdGeAs_2$ is at least 10 times that of the hole mobility.[20] The square of the mobility ratio determines this effect, allowing the switch to occur while the electron concentration is still one to two orders of magnitude less than the hole concentration. When this effect is observed, the following equation relates the total concentrations of acceptor impurities ($N_a$) in the material to the carrier density:

$$N_a = \frac{p}{1 - R - \dfrac{1}{\dfrac{1}{2}\exp\left(\dfrac{E_F - E_a}{k_B T}\right)} + 1}$$

where R is the compensation ratio listed in Table II, and the Fermi level, $E_F$, is determined from the mobility ratio and effective masses through the standard formula for the intrinsic carrier concentration.[21] Since there is uncertainty in the material properties necessary for this calculation, particularly in the band gap and the effective masses of holes and electrons, the values of $N_a$ determined in this way must be viewed as approximate. Values of $N_a$ are listed in Table III, determined when the transition in conductivity was observed. These calculations have assumed[18] a ratio for the electron-to-hole mobility of 12, and effective masses based on the theoretical work of Borisenko *et al.*[22]

Four point resistivity measurements were performed on the $c_{||}$ sample from each sample set, allowing the resistivity anisotropy to be directly measured. Representative temperature-dependent resistivity measurements (for sample set 49) are shown in Figure 15. The resistivity anisotropy is also summarized in Table III. If we assume that the a-axis mobilities of the two matched samples are the same, which is reasonable since they were cut from the same area in the boule, then the anisotropy in resistivity determines the mobility parallel to the c-axis. The highest a-axis p-type mobility directly measured in these samples was ~260 $cm^2$/V-sec, and the highest measured a-axis n-type mobility was ~1500 $cm^2$/V-sec. For samples exhibiting type conversion, the n-type mobility had not yet saturated within the limits of our measurements. It should also be noted that the electrical contacts became blocking for the less conductive samples at lower temperatures, limiting the temperature range of the Hall measurements.

**Table III. Results of Hall measurements in $CdGeAs_2$.**

| Sample | RT ρ Anisotropy | a-axis Mobility ($cm^2$/V-sec) | c-axis Mobility ($cm^2$/V-sec) | $N_a$ Estimate ($cm^{-3}$) | Maximum Mobility ($cm^2$/V-sec) | Temperature for Maximum Mobility (K) |
|---|---|---|---|---|---|---|
| 29 | 340 | 178 | 60520 | $3x10^{16}$ | 245 | 170 |
| 30 | 14.7 | 210 | 3087 | $1x10^{17}$ | 245 | 170 |
| 31 | 2.7 | 140 | 378 | - | 146 | 250 |
| 34 | 4 | 910 | 3640 | - | 1500($\mu_e$) | 400 |
| 37 "dark" | 3.6 | 124 | 446 | $>10^{18}$ | 120 | 250 |
| 37 "light" | 4 | 155 | 620 | $2x10^{17}$ | 210 | 185 |
| 49 | 40 | 165 | 6600 | $3x10^{16}$ | 225 | 190 |
| 50 | (a) | (b) | (a) | $5x10^{15}$ | 150, 1500($\mu_e$) | 185, 400 |
| 51 | 2.2 | 149 | 328 | $1x10^{17}$ | 240 | 180 |

(a) Not measured (b) Not reliable due to proximity to Hall coefficient transition

Early in this study it was recognized at Sanders that the infrared absorption varied strongly from place to place within a given boule, occasionally with a sharp transition zone. Two sample sets (labeled 37) were cut for Hall analysis on either side of one such transition, one termed the "light" set due to its relative lack of absorption, and the other termed the "dark" set for its higher level of absorption. Electrically, as well as optically, the two sets were quite different. The "light" set was much less conductive due to a mixture of higher compensation and lower $N_a$, with the measured acceptor energy level somewhat larger that its "dark" counterpart, 125 vs. 109 meV. This trend in electrical properties is consistent with the results of absorption coefficient measurements for the four undoped sample sets, as indicated by the data in Table II. In order to better understand the origin of this difference in electrical and optical properties, more must be known about the impurities in the material. Seven of the nine sample sets investigated were pre-selected based on optical absorption measurements.

Of particular interest are the high values for the c-axis mobility, with one reaching above 60,000 $cm^2$/V-sec. These are not artificial values, as the error involved in measuring the a-axis resistivity ratio of these sets cannot account for the high mobilities. The ratio is roughly constant over all temperatures investigated, even though each resistivity varied by five orders of magnitude. These measurements have been repeated to further establish their validity. Work is underway to directly measure the c-axis mobility of material from these boules by using a standard Hall bar geometry.

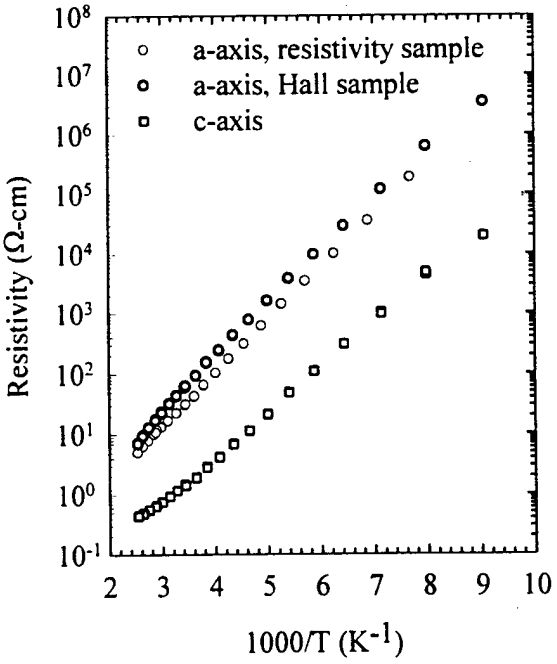


Figure 15. Resistivity anisotropy for sample set 49.

Samples that were intentionally doped were done so with the donor dopants selenium and tellurium, the acceptor dopant silver, and chromium which is expected to be a deep level. The Cr, Ag, Te and lightly Se-doped samples exhibited few differences. They were all p-type with carrier densities of ~1-2 x $10^{15}$ $cm^{-3}$ at room temperature, and they appeared to be dominated by the background p-type doping. The doped samples had acceptor activation energies that ranged from 130 to 150 meV which were more likely due to native defects and residual impurities than to intentional dopants. The only real distinction between these samples was in the ratio of the c- and a-axis resistivities, which also may be coincidental. This ratio ranged from ~2 for the Te-doped set to ~340 for the Cr doped samples. The higher conductivity for the c-axis is related to the smaller effective mass, and thus higher mobility, along this direction. The mobility is related to the scattering lifetime as well as the effective mass. Any isotropic scattering process, such as ionized impurity scattering, will tend to "homogenize" the mobility thereby lowering the anisotropy. It is interesting that the samples with the larger resistivity anisotropy also had the lowest estimated concentrations of background acceptors.

Sample set 34 was highly doped with Se, and was n-type at room temperature with an electron density of ~$9x10^{16}$ $cm^{-3}$ which did not change appreciably over the temperature range measured, ~ 200 to 400 K. It proved difficult to make contacts with indium to the n-type samples that performed below ~220 K. The carrier concentration over this temperature range showed no evidence of carrier "freeze-out" resulting in an upper limit for the donor activation energy of ~20 meV below the conduction band. It is likely that this sample was highly compensated, assuming the sample had the same background acceptor levels as the others measured. This was consistent with the steadily decreasing electron mobility measured with decreasing temperature at all temperatures investigated, indicating significant ionized impurity scattering.

Previous studies[17,18] indicate a clear demarcation between activation energies for extrinsic acceptors (120 to 130 meV) and native defects (150 to 160 meV) in $CdGeAs_2$. The differences in the activation energies from sample to sample can be understood by considering the possibility of two separate acceptor levels. Predicted carrier concentrations were generated using the appropriate charge-balance models[23] with known parameters for two acceptors, then fit with the single acceptor model used for all of the above samples in order to test the validity of this assumption. The data were generated assuming that there were two acceptor levels, one lying at 120 meV ($N_{a120}$) and the other at 160 meV ($N_{a160}$), completely ionized donors, and a total compensation ratio of 0.70. The data generated in this way can be fit quite well by the single acceptor model as seen in Figure 16. For the

two cases where the concentration of one level is 100 times larger than the other, the fit using the single acceptor model returns the values attributed to that level ($N_d/N_a$~0.70 and $E_a$~0.160meV for the squares and $N_d/N_a$~0.69 and $E_a$~0.121meV for the triangles.) When the levels are equally abundant, the fit is dominated by the deeper level ($N_d/N_a$~0.61 and $E_a$~0.152meV for the circles). If the more shallow level is associated with extrinsic impurities, then we should measure the smaller activation energy only for those samples with a high concentration of impurities that greatly exceed intrinsic acceptors. As can be seen by comparing Table II and Table III, samples with a shallower acceptor level tend to have a significantly higher total concentration of impurities. Thus, it can be seen that the wide range of acceptor energies often observed is consistent with the presence of at least two distinct acceptor energy levels.

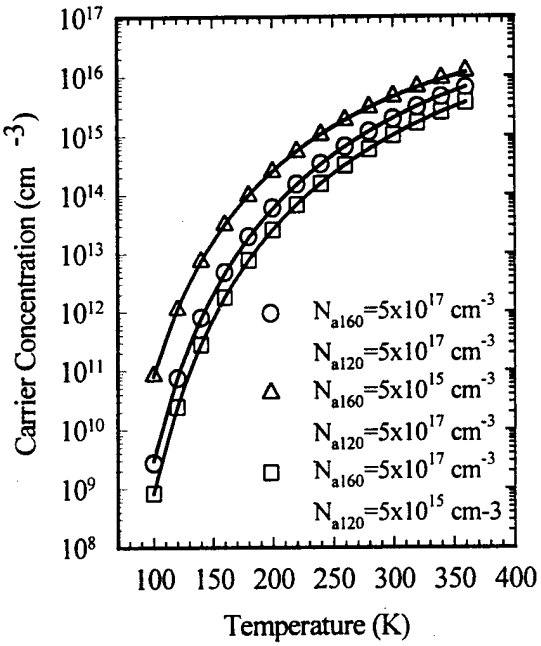


Figure 16. Generated data based on a two acceptor level, one shallow donor model and their corresponding one acceptor level fits.

In conclusion, several sets of $CdGeAs_2$ samples have been measured and analyzed by temperature-dependent Hall effect. N-type conduction was only obtained with high levels of doping, with electrical measurements indicating that Se is a shallow donor. Both undoped and less heavily-doped samples grown with the deliberate introduction of Se, Te,

Cr and Ag show similar electrical properties dominated by the background p-type doping, with a wide range of acceptor energies observed. All of the p-type results are consistent with a model employing a single shallow donor and at least two separate acceptor levels. An intriguing mobility has been observed along the c-axis that is still under investigation.

## III. RESULTS OF POINT DEFECT STUDIES IN KTP CRYSTALS

Potassium titanyl phosphate ($KTiOPO_4$), better known as KTP, is an important nonlinear laser material.[24-26] It has many excellent optical and physical properties and is presently used in second harmonic generation (SHG) and optical parametric oscillator (OPO) devices. However, laser-induced damage[27-32] continues to be a problem in some of these applications. Gray tracks, regions of increased visible absorption, may form along the beam path in the bulk of a KTP crystal when the pump laser operates at high peak power. Once formed, these absorption bands can significantly degrade the performance of a device. The susceptibility to gray tracking is known to vary from one KTP crystal to another and this strongly suggests that extrinsic electron and hole traps are a major factor in the damage mechanism. Arriving at a detailed understanding of the gray-track phenomenon thus requires a complete identification and characterization of all of the electron and hole traps present in KTP crystals. This AFOSR project is intended to evaluate important optically active point defects in KTP and define their relation to laser-induced damage.

### A. PLATINUM-ASSOCIATED ELECTRON AND HOLE TRAPS

In the present section, we describe the results of an EPR investigation of three platinum centers induced in hydrothermally grown KTP by ionizing radiation. Although our study focused on hydrothermally grown material, we have observed these same platinum centers in flux-grown crystals. Complete g matrices and $^{195}Pt$ hyperfine matrices are reported for each of the three centers. The center labeled Pt(A) is assigned to a $Pt^{3+}$ ion substituting for a $Ti^{4+}$ ion. The centers labeled Pt(B) and Pt(C) have a quite different behavior and are suggested to be $Pt^{+}$ ions substituting for $K^{+}$ ions. In this scheme, Pt(A) is a trapped electron center (i.e., it is a $Pt^{4+}$ ion before irradiation) and Pt(B) and Pt(C) are trapped hole centers (before irradiation, they are believed to be neutral $Pt^{0}$ atoms).

The structure[33] of KTP is orthorhombic (space group $Pna2_1$) with a = 12.819 Å, b = 6.399 Å, and c = 10.584 Å. There are 64 atoms in the unit cell; these can be separated into four sets of 16 atoms which transform into each other according to the symmetry

elements of the crystal. In general, the KTP lattice has two inequivalent titanium sites, two inequivalent potassium sites, two inequivalent phosphorus sites, and ten inequivalent oxygen sites. Additional information about this crystal structure is provided in Ref. 34.

The KTP sample used in the present investigation was grown by the high-temperature hydrothermal method at Litton-Airtron (Charlotte, NC). This particular crystal was selected because it contained a larger than usual concentration of platinum, estimated from the intensity of the EPR signals to be approximately two ppm, and a smaller than usual concentration of transition-metal ions (i.e., $Fe^{3+}$ and $Cr^{3+}$). Platinum is a trace impurity in many KTP crystals because platinum crucibles are used to prepare starting materials used in growth. Dimensions of the EPR sample were 1.5 x 1.3 x 3.5 $mm^3$. In this study, the platinum impurities were converted to a paramagnetic form by irradiating for one hour at room temperature with x-rays from a tube operating at 55 kV and 28 mA. For x-ray irradiations at 77 K, the sample was held in a styrofoam cup filled with liquid nitrogen and then quickly transferred into the EPR spectrometer. The 355-nm tripled output of a pulsed Nd:YAG laser was used to optically induce the paramagnetic platinum centers at room temperature.

A Bruker ESP 300 spectrometer operating at 9.452 GHz was used to obtain the EPR data. The sample temperature was controlled using an Oxford Instruments Model ESR-900 helium-gas flow system. A Varian E-500 digital NMR gaussmeter was used to measure the magnetic field and a Hewlett-Packard 5340A counter was used to measure the microwave frequency. An MgO crystal doped with Cr was used to correct for the difference in magnetic field between the KTP sample and the gaussmeter probe (the isotropic g value of $Cr^{3+}$ in MgO is 1.9800).

Platinum impurities in as-grown KTP crystals are not paramagnetic (i.e., EPR spectra attributable to platinum are not observed initially). The EPR spectra which are present in as-grown crystals are due to $Fe^{3+}$ and $Cr^{3+}$ ions substituting for $Ti^{4+}$ ions. [35-37] After an x-ray irradiation at room temperature, we observed three paramagnetic platinum centers in our hydrothermally grown KTP sample. Their EPR spectra are shown in Figure 17. These data were taken at 30 K with the magnetic field parallel to the b axis of the crystal. Exposure to a 355-nm laser beam at room temperature produces the same defects. Each of the three centers, which we have arbitrarily labeled Pt(A), Pt(B), and Pt(C), consists of a central line surrounded by a less intense pair of hyperfine-split lines. This three-line pattern for each center is easily explained by the natural abundance of the $^{195}Pt$ nucleus (I = 1/2, 33.8% abundant). Interestingly, the Pt(A) centers exhibit a well- resolved

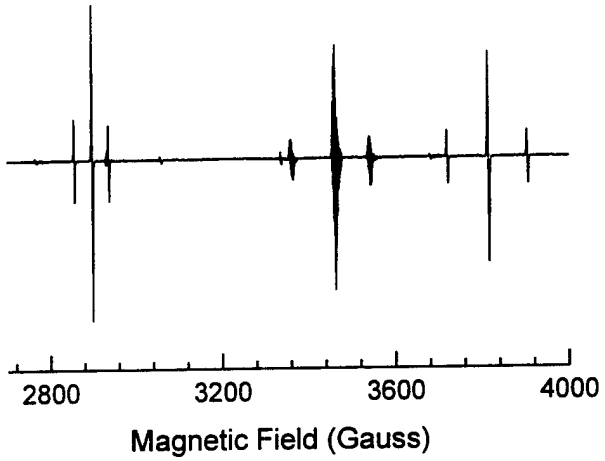


Figure 17. EPR spectrum showing three platinum centers produced by an x-ray irradiation at room temperature. These data were taken at 30 K with the magnetic field parallel to the b axis of the crystal. The microwave frequency was 9.452 GHz.

superhyperfine structure, as illustrated in Figure 18. These data in Figure 18 are an expansion of the center signal of the Pt(A) center in Figure 17. We attribute these additional splittings to neighboring phosphorus nuclei, in analogy with the phosphorus hyperfine always exhibited by the various $Ti^{3+}$ centers in KTP. [38,39] In contrast, Pt(B) and Pt(C) centers show no resolved superhyperfine structure (their EPR linewidths are approximately 2 gauss).

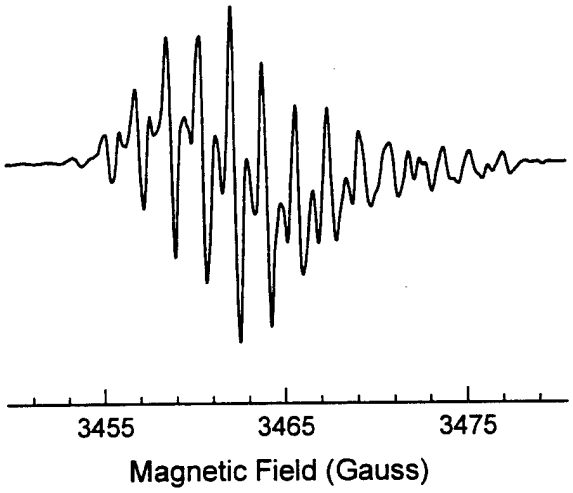


Figure 18. Superhyperfine structure associated with the central EPR line of the Pt(A) center. The data were taken at 30 K, the magnetic field was parallel to the b axis of the crystal, and the microwave frequency was 9.452 GHz. Some of the weaker lines on the high field side may be due to a separate center.

The three platinum centers represented by the EPR spectra in Figure 17 were produced during an irradiation at room temperature. These same three centers are also formed during an x-ray irradiation at 77 K, but with different relative intensities. After irradiating at room temperature, the concentration of Pt(A) centers is approximately the same as the combined concentrations of Pt(B) and Pt(C) centers. Whereas after irradiating at 77 K, followed by a transfer to the EPR cavity without warming, the concentration of Pt(A) centers is large, and the concentrations of Pt(B) and Pt(C) centers are very small. During a subsequent anneal to room temperature after the irradiation at 77 K, the Pt(B) and Pt(C) centers increase in concentration and the Pt(A) centers decrease significantly in concentration. In earlier 77-K irradiation studies, the presence of the center now referred to as Pt(A) was reported by Scripsick et al.[40] and the growth upon annealing of centers now referred to as Pt(B) and Pt(C) was described by Scripsick et al.[41]

The rates of decay of the three paramagnetic platinum centers were measured for an anneal temperature of 120°C. After an x-ray irradiation at room temperature, the sample was cooled to 30 K where the intensities of the EPR signals from the three centers were monitored. Then the sample was heated to 120°C and held for a fixed period of time (5 min). Following the anneal step, the sample was returned to 30 K where the EPR signals were again measured. This cycle was repeated a number of times, with increasing periods of anneal time, until negligible concentrations of each center remained. The Pt(B) centers were reduced to approximately one-half of their initial concentration after 15 min of anneal time at 120°C. The Pt(A) and Pt(C) centers have very similar thermal decay behaviors, and they decay much more slowly than the Pt(B) centers. The Pt(A) and Pt(C) centers required approximately 90 min of anneal time at 120°C to be reduced to one-half of their initial concentration. These platinum centers have decay times of several weeks or longer when the crystal is held at room temperature after an irradiation at room temperature.

Figures 19, 20, and 21 show the angular dependence of the Pt(A), Pt(B), and Pt(C) centers, respectively. Data were taken at 30 K in all three crystal planes, with careful attention given to maintaining the magnetic field within the crystal planes during rotations. For an arbitrary direction of the magnetic field, there are four magnetically inequivalent, but crystallographically equivalent, orientations of each platinum center in the KTP lattice. If the magnetic field is restricted to the a-c, b-c, or a-b planes (as in Figures 19, 20, and 21), the four sites become pairwise degenerate. All four sites are degenerate when the magnetic field is along the highest symmetry directions (i.e., the crystal axes). In Figures 19, 20, and 21, the discrete points represent experimental data and the solid lines were computer-generated using final values of the spin-Hamiltonian parameters. More than 200

data points were collected for each platinum center. In addition to the data taken in the three planes, one measurement of line positions was made at an orientation well away from any of the three planes.

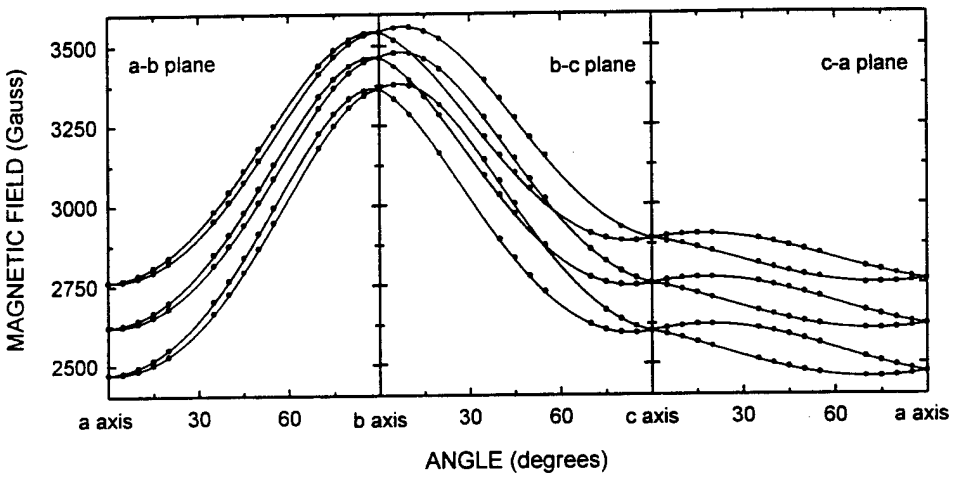


Figure 19. Angular dependence of the Pt(A) center. Discrete points are experimental EPR data and the solid curves are computer-generated using the "best fit" parameters.

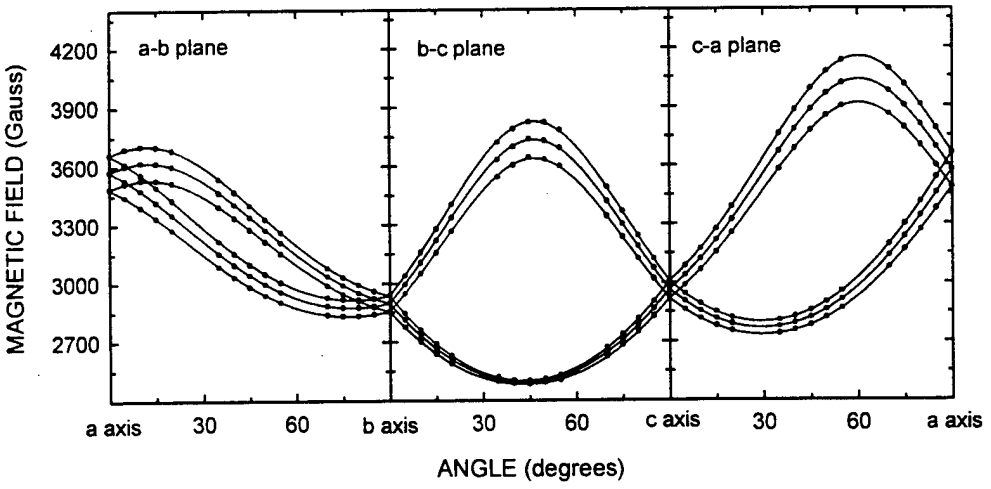


Figure 20. Angular dependence of the Pt(B) center. Discrete points are experimental EPR data and the solid curves are computer-generated using the "best-fit" parameters.

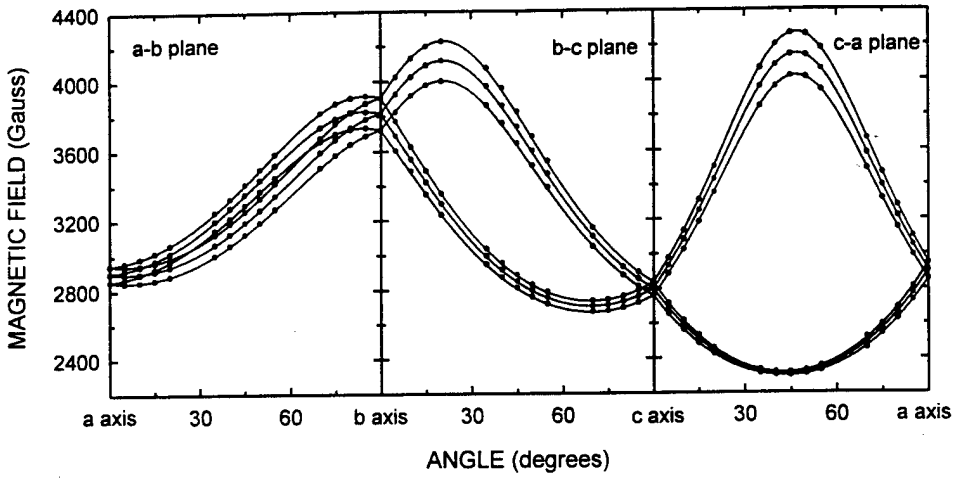


Figure 21. Angular dependence of the Pt(C) center. Discrete points are experimental EPR data and the solid curves are computer-generated using the "best-fit" parameters.

The following spin-Hamiltonian was used to analyze the angular dependence of each platinum center.

$$\mathbf{H} = \beta \mathbf{B}\cdot\mathbf{g}\cdot\mathbf{S} + \mathbf{S}\cdot\mathbf{A}\cdot\mathbf{I} - g_N\beta_N\mathbf{B}\cdot\mathbf{I}$$

The electron Zeeman, the platinum hyperfine, and the nuclear Zeeman interactions are represented by the three terms. No attempt was made to analyze the superhyperfine associated with the Pt(A) center, so this term was not included. The **g** matrix and the hyperfine **A** matrix each require six parameters for a complete description (i.e., three principal values and three Euler angles for the principal directions). Thus, there are a total of twelve parameters to be determined for each center. A least-squares fitting program utilizing exact diagonalizations of the matrix form of the above Hamiltonian was used to obtain the "best" values of these parameters. The results for the Pt(A), Pt(B), and Pt(C) centers are listed in Table IV. We have used our one measurement of EPR line positions at an out-of-plane orientation to determine the correct set of parameters for each matrix, from a choice of two sets which equally well fit the in-plane data. The Euler angles have been converted to pairs of angles ($\theta$, $\phi$), where the polar angle $\theta$ is measured relative to the c axis and the azimuthal angle $\phi$ is measured relative to the a axis in the c plane with positive rotation from a to b. In Table IV, the given directions of the principal axes correspond to one of the four possible sites for each center. The principal-axis directions for the other three sites are obtained by applying the symmetry elements of the lattice.[34]

| Pt(A) | Pt(B) | Pt(C) |
|---|---|---|
| $g_1 = 1.9397$ | $g_1 = 1.6019$ | $g_1 = 1.4656$ |
| $g_2 = 2.4463$ | $g_2 = 1.9754$ | $g_2 = 1.8597$ |
| $g_3 = 2.5900$ | $g_3 = 2.7788$ | $g_3 = 2.9576$ |
| $A_1 = 479$ MHz | $A_1 = 47$ MHz | $A_1 = 69$ MHz |
| $A_2 = 956$ MHz | $A_2 = 379$ MHz | $A_2 = 388$MHz |
| $A_3 = 1081$ MHz | $A_3 = -613$ MHz | $A_3 = 673$ MHz |

Table IV. Principal values of the g matrices and the platinum A matrices for the Pt(A), Pt(B), and Pt(C) centers in KTP. Parameter values are given for one site of each center. Error limits on the g principal values and hyperfine principal values are estimated to be ±0.0005 and ±2.0, respectively.

The three observed paramagnetic platinum centers, arbitrarily labeled Pt(A), Pt(B), and Pt(C), can be separated into two groups according to their characteristics and behavior. One group contains the Pt(A) center and the other group contains the Pt(B) and Pt(C) centers. Among the distinguishing factors are superhyperfine structure, nature of the g matrix, production at 77 K, and thermal anneal between 77 K and room temperature. For example, the Pt(A) center exhibits a clear superhyperfine structure due to nearby phosphorus ions, but the Pt(B) and Pt(C) centers show no superhyperfine structure. From examination of the g matrices, we see that the Pt(A) center has a g matrix which is close to axial (with $g_{||} \approx 2$ and $g_{\perp} > g_{||}$), while the Pt(B) and Pt(C) centers have nonaxial g matrices with large shifts, both positive and negative, relative to $g = 2$. An irradiation at 77 K produces many more Pt(A) centers than Pt(B) and Pt(C) centers, but an anneal from 77 K to room temperature increases the Pt(B) and the Pt(C) centers and destroys a significant portion of the Pt(A) centers. Finally, we note that the combined concentration of Pt(B) and Pt(C) centers following a room-temperature irradiation is approximately equal to the concentration of Pt(A) centers.

The results described in the preceding paragraph can be understood if during an irradiation the Pt(A) center is formed by trapping an electron and the Pt(B) and Pt(C) centers are formed by trapping a hole. This requires the precursor of the Pt(A) center to be different from the precursor of the Pt(B) and Pt(C) centers. In general, platinum impurities can occupy (with different charge states) both the titanium and the potassium sites in the KTP lattice. A $Pt^{4+}$ ion ($5d^6$) can readily substitute for a $Ti^{4+}$ ion, and convert to a $Pt^{3+}$ ion ($5d^7$) when it traps an electron. It is also possible that a $Pt^0$ atom ($5d^{10}$) could

substitute for a $K^+$ ion, and convert to a $Pt^+$ ion ($5d^9$) when it traps a hole. In each case, the platinum is in a nonparamagnetic state initially and becomes paramagnetic after an irradiation (i.e., by trapping either the electron or the hole).

Support for the assignment of the Pt(A) center to a $Pt^{3+}$ ion substituting for a $Ti^{4+}$ ion comes from the g matrix for this defect, which is very similar to the g matrices reported earlier for $Pt^{3+}$ ions ($5d^7$) substituting for sixfold coordinated cations in a variety of crystals, including $BaTiO_3$, MgO, and $PbWO_4$.[42-44] In contrast, the larger shifts and nonaxial nature of the g matrices for the Pt(B) and Pt(C) centers are consistent with the large crystalline electric field and the low symmetry experienced by $Pt^+$ ions ($5d^9$) substituting for $K^+$ ions. Having two centers with similar properties, i.e., Pt(B) and Pt(C), occurs because the two crystallographically inequivalent $K^+$ sites in the KTP lattice both contain $Pt^+$ ions.

When a KTP crystal is exposed to ionizing radiation at 77 K (as opposed to room temperature), a large number of "free" holes become trapped on oxygen ions adjacent to potassium vacancies.[34, 45] In most KTP crystals, there is a very high concentration of potassium vacancies (much larger than the platinum concentration). Thus, at 77 K, radiation-induced holes are much more likely to be trapped by the potassium vacancies than by the smaller concentration of $Pt^0$ ions substituting for $K^+$ ions. The trapped-hole centers associated with potassium vacancies are not formed by a room-temperature irradiation, since they are unstable above approximately 160 K. We suggest that this competition among trapping sites at low temperature is the reason fewer Pt(B) and Pt(C) centers are formed at 77 K, as compared to room temperature. During an anneal from 77 K to room temperature, holes will be released from the potassium-vacancy-associated hole centers and migrate through the lattice. The Pt(A) centers will trap some of these migrating holes (i.e., the hole will recombine with the trapped electron) and the concentration of Pt(A) centers will decrease. At the same time, the $Pt^0$ ions also will trap some of the migrating holes and the concentrations of Pt(B) and Pt(C) centers will increase. This decrease in Pt(A) centers and increase in Pt(B) and Pt(C) centers during an anneal from 77 K to room temperature is in agreement with experiment.

A KTP crystal which contains large concentrations of platinum impurities will be more susceptible to the formation of gray tracks than crystals with higher purity. These gray tracks are regions of high absorption formed along the path of an intense laser beam, and the coloration is associated with the trapping of electrons and holes at defects. When platinum is present, it provides additional trapping sites for the electrons and holes

generated by the laser beam. Although no absorption bands have been attributed directly to the platinum centers, their ability to trap charge may enable other absorbing centers such as $Ti^{3+}$ and $Fe^{4+}$ ions to form in KTP when it is used in high-power nonlinear applications.

In summary, electron paramagnetic resonance (EPR) techniques have been used to characterize three platinum centers in a hydrothermally grown KTP crystal. These centers can be produced by x-rays or laser beams at room temperature, but their EPR spectra can only be observed at temperatures near or below 30 K. We have arbitrarily labeled them Pt(A), Pt(B), and Pt(C). The Pt(A) center is a $Pt^{3+}$ ion ($5d^7$) substituting for a $Ti^{4+}$ ion. It is formed when a $Pt^{4+}$ ion at the titanium site traps an electron and is converted to the paramagnetic $Pt^{3+}$ ion. The Pt(B) and Pt(C) centers are suggested to be $Pt^{+}$ ions ($5d^9$) substituting for $K^{+}$ ions. They are formed when a $Pt^{0}$ atom at a potassium site traps a hole. The two distinct hole-trapping centers, Pt(B) and Pt(C), correspond to the two crystallographically inequivalent potassium sites. Although our present study was focused on platinum defects in a hydrothermally grown crystal, we have observed the same platinum centers in flux-grown KTP crystals. The ability of platinum impurities to serve as electron traps or hole traps, depending on which lattice site is occupied, allows them to play a role in the formation of gray tracks when the KTP crystals are used in high-power frequency-doubling applications.

## B. SILICON-ASSOCIATED HOLE TRAP

In the present section, we describe the role of silicon impurities as hole traps in KTP. Both x-rays and 355-nm laser beams are shown to produce, at room temperature, an electron paramagnetic resonance (EPR) spectrum which is assigned to a silicon-associated trapped-hole center. The silicon ions substitute for phosphorus and readily trap a hole on an adjacent oxygen ion during irradiation. An EPR angular study of this center at room temperature provides the principal values and principal axes of the g-matrix. Additional EPR data, taken at 25 K, show that the corresponding electron center induced by the x-rays or the laser beam is a $Ti^{3+}$ ion, specifically Center A which had been previously characterized by Roelofs.[27] The silicon-associated hole centers decay near room temperature as a result of the release of electrons from the $Ti^{3+}$ centers. This process is shown to follow primarily second-order kinetics and a "frequency" factor and activation energy are obtained from decay data taken at three temperatures.

We note that the holelike EPR spectrum described in the present section has been reported in an earlier work by Karaseva et al.[46] They assigned the spectrum to a $(PO_4)^{2-}$ center and suggested that it is formed when a hole is trapped by a regular $(PO_4)^{3-}$ unit in the unperturbed lattice. This assignment by Karaseva et al.[46] is, however, questionable for two reasons. First, their model suggests that the hole is trapped in the otherwise perfect lattice (i.e., a self-trapped hole) since no stabilizing entity such as a cation vacancy or an impurity is proposed. No self-trapped hole center has yet been demonstrated to exist as a stable defect in an oxide crystal.[47] Second, their reported hyperfine interaction with the primary phosphorus nucleus is very anisotropic, varying from 1.5 to 9 G. This appears to be too small an interaction to support their proposed model of a $(PO_4)^{2-}$ center. We bring attention to an analogous $(PO_4)^{2-}$ trapped hole center in $KH_2PO_4$ crystals[48] which is associated with a hydrogen vacancy and has a predominantly isotropic 32-G hyperfine interaction with the primary phosphorus nucleus. For these reasons as well as others presented in the following sections, we propose that the holelike center initially observed by Karaseva et al.[46] in KTP is a result of silicon impurities replacing phosphorus ions.

The KTP crystals used in this project were grown by the flux technique at Crystal Associates (East Hanover, NJ). A $K_6P_4O_{13}$ flux was used and a typical growth run lasted approximately 30 days as the temperature was reduced from about 920°C to 870°C. One crystal was doped during growth by adding one mole percent of silicon to the starting materials. All other crystals were undoped. Dimensions were 2 x 3 x 5 $mm^3$ for the EPR samples and 2 x 8 x 8 $mm^3$ for the optical samples. In each case, the sample faces were perpendicular to the **a**, **b**, and **c** crystal axes. The structure[33] of KTP is orthorhombic (space group $Pna2_1$) with a = 12.819 **Å**, b = 6.399 **Å**, and c = 10.584 **Å**. A description of this crystal structure, including crystallographically inequivalent sites for the constituent atoms, is presented in Reference 34.

Two distinctly different sources of ionizing radiation were used to produce the paramagnetic defects at room temperature in our KTP crystals. One was an x-ray tube operating at 60 kV and 30 mA, while the other was the tripled output (355-nm) from a Nd:YAG laser (Continuum Powerlite 8000). These 355-nm photons easily form pairs of electrons and holes since their energy exceeds the 360-nm band edge of KTP at room temperature. The laser operated at a 10 Hz repetition rate with a pulse width of 10 ns, and the energy per pulse in the tripled beam was 150 mJ. The fundamental (1064 nm) and the doubled (532 nm) output beams were not incident on the crystal during the exposures to the 355-nm photons.

Ionizing radiation, such as the x-rays or the 355-nm laser beam, will randomly produce electrons and holes in the otherwise perfect KTP lattice. Many of these electrons and holes will immediately recombine, radiatively or nonradiatively, to restore the original lattice; however, a portion of the electrons and holes will migrate sufficiently far from each other and encounter a stabilizing entity, such as a vacancy or an impurity. This allows a few of the electrons and holes to become stabilized at widely separated sites in the crystal and form the point defects that contribute to the induced visible optical absorption (i.e., gray tracking). In general, holes will be trapped at transition-metal ions,[31] such as Fe and Cr, or they will be localized on oxygen ions adjacent to stabilizing entities such as potassium vacancies[34] or silicon ions substituting for phosphorus. Electrons, on the other hand, will be localized on titanium ions, thus forming $Ti^{3+}$ centers, with a neighboring $OH^-$ ion or oxygen vacancy providing the trapping potential.[27,38]

In their as-grown state (i.e., before irradiation), all of our KTP crystals exhibited EPR spectra due to $Fe^{3+}$ and $Cr^{3+}$ impurities.[35-37,49-50] After exposure to x-rays or a 355-nm laser beam at room temperature, most of these $Fe^{3+}$ and $Cr^{3+}$ signals decrease and other EPR signals appear. Of the new EPR spectra induced by the x-rays or the laser beam, we find that some can be monitored at room temperature while others can only be seen at lower temperatures. For example, Figure 22 shows the EPR spectrum of a silicon-doped crystal after being x-irradiated for one hour at room temperature. These data were taken at room temperature, the magnetic field was parallel to the a axis of the crystal, and the microwave frequency was 9.666 GHz. The same spectrum is present in undoped KTP after an x-irradiation and is also found in both undoped and silicon-doped samples after exposure to the 355-nm laser beam. The single line near 3434 G in Figure 22 is the holelike EPR signal previously reported by Karaseva et al.[46] We estimate the concentration of this center to be approximately $4 \times 10^{15}$ $cm^{-3}$. The two sets of lines near 3520 G in Figure 22 may be due to $Cr^{5+}$ centers located at crystallographically inequivalent sites (e.g., the Ti(1) and Ti(2) sites). These latter lines require further investigation before an absolute identification can be made and they will not be discussed in the present section.

Room-temperature irradiation of our KTP samples with x-rays or a 355-nm laser beam produced the four $Ti^{3+}$ centers originally reported by Roelofs.[27] It is important to note that although these electron traps may be present at room temperature, their EPR spectra can be observed only near or below 77 K. A previous study has suggested that each

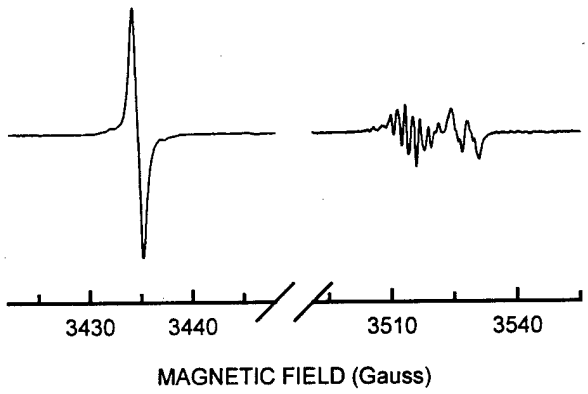


Figure 22. EPR spectrum of a silicon-doped KTP crystal taken at room temperature with the magnetic field parallel to the a axis. The crystal has been x-irradiated at room temperature. The silicon-associated hole center is at lower field and two $Cr^{5+}$ centers (multiplied by a factor of five) are at higher field.

of these $Ti^{3+}$ centers is located adjacent to an oxygen vacancy.[38] We found that Center A (in Roelofs' notation) is the dominant center after an irradiation at room temperature; it has a concentration at least twenty times greater than any of the other three $Ti^{3+}$ centers.[31] Figure 23 shows the EPR spectrum of Center A in a silicon-doped crystal that had been x-irradiated for one hour at room temperature. These data were taken at 25 K, the magnetic field was parallel to the c axis of the crystal, and the microwave frequency was 9.494 GHz. The structure in Figure 23 results from the hyperfine interactions of the $Ti^{3+}$ ion with four neighboring phosphorus nuclei (a result verified by a recent electron-nuclear double resonance (ENDOR) investigation[51] performed in our laboratory). Roelofs resolved the hyperfine from only two of these neighboring phosphorus nuclei in his initial study. A modulation frequency of 25 kHz, instead of the usual 100 kHz, was used to obtain the well-resolved hyperfine pattern shown in Figure 23. This lower modulation frequency minimized broadening effects due to a temperature-dependent spin-lattice relaxation time.

There are no measurable optical absorption bands present in the KTP crystals prior to their exposure to the x-ray beam or the 355-nm laser beam. After exposure to x-rays for one hour at room temperature, the silicon-doped KTP crystals become visibly colored. This induced optical absorption is illustrated in Figure 24 where spectra taken before and immediately after an x-irradiation at room temperature are shown. There is a broad band peaking near 500 nm and extending throughout the visible, from beyond 750 nm to the crystal's band edge at 360 nm. This absorption may have contributions from both the

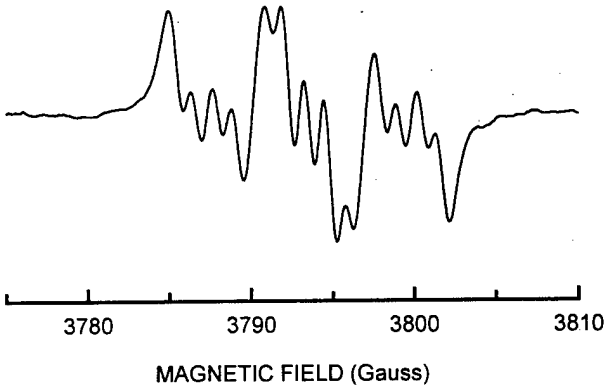


Figure 23. EPR spectrum of a silicon-doped KTP crystal taken near 25 K with the magnetic field parallel to the a axis. The crystal has been x-irradiated at room temperature. This set of hyperfine-split lines is attributed to Center A, a $Ti^{3+}$ electron trap previously reported by Roelofs (Reference 27).

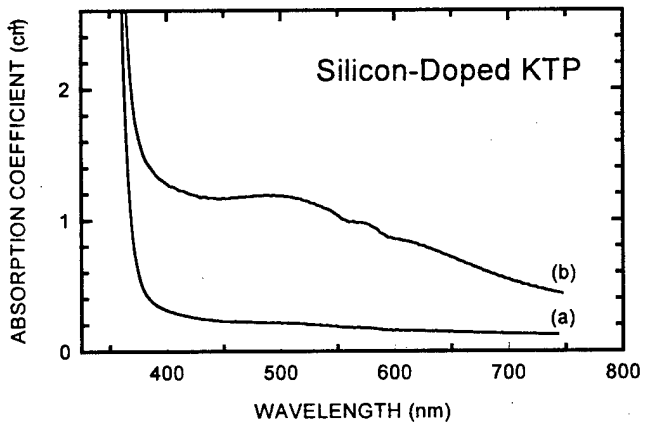


Figure 24. Optical absorption spectra of a silicon-doped KTP crystal taken at room temperature before (a) and after (b) x-irradiation at room temper-ature. The two small features in trace (b) between 550 and 600 nm are spurious responses of the spectrophotometer.

trapped hole center and the $Ti^{3+}$ centers. An identical absorption spectrum, except reduced in intensity by a factor approaching ten, is found in the undoped KTP samples after they are x-ray irradiated at room temperature. Also, this same absorption band is induced in silicon-doped and undoped crystals at room temperature by the 355-nm laser.

The holelike EPR signal occurring near 3434 G in Figure 22 is present in all the flux-grown KTP crystals examined in the present project. Its concentration varies by factors of two or three in the undoped samples. However, in a silicon-doped sample, its concentration is an order of magnitude greater than the average value found for the undoped samples. This significant enhancement in intensity in a silicon-doped crystal has led us to assign the EPR spectrum to a silicon-associated trapped hole center. When a silicon ion ($Si^{4+}$) substitutes for a phosphorus ion ($P^{5+}$) in KTP, an extra positive charge is needed to maintain electrical neutrality. This is most easily accomplished by trapping a hole on an oxygen adjacent to the silicon ion. A thermal stability near room temperature and a lack of significant hyperfine structure also support this assignment. There is a weak pair of lines, split by approximately five gauss and centered on the EPR signal in Figure 22, which we suggest is due to a $^{29}Si$ nucleus (4.7% abundant, I = ½). An analogous center in α-quartz consists of an aluminum ion ($Al^{3+}$) substituting for a silicon ion ($Si^{4+}$) with a hole trapped on an adjacent oxygen ion.[52] It is of interest to note that the silicon ions which trap holes in our KTP samples occupy only one of the two possible inequivalent phosphorus sites.

A detailed investigation of the angular dependence of the silicon-associated hole center in KTP has been completed. Data were taken at $10^{o}$ intervals in each of the three high symmetry planes of the crystal, as shown in Figure 25. For an arbitrary direction of the magnetic field, there are four magnetically inequivalent, but crystallographically equivalent, orientations of the hole center. If the magnetic field is restricted to the a-c, b-c, or a-b planes, the four sites become pairwise degenerate. All four sites are degenerate when the magnetic field is along a high-symmetry direction (i.e., one of the crystal axes) and the EPR spectrum then consists of a single line. The "effective" g values for the high-symmetry directions are $g_a = 2.0110$, $g_b = 2.0029$, and $g_c = 2.0313$. For our silicon-associated hole center, the pairwise splitting expected in the a-b plane does not occur (see Figure 25) and only a single line is observed for all orientations of magnetic field in this

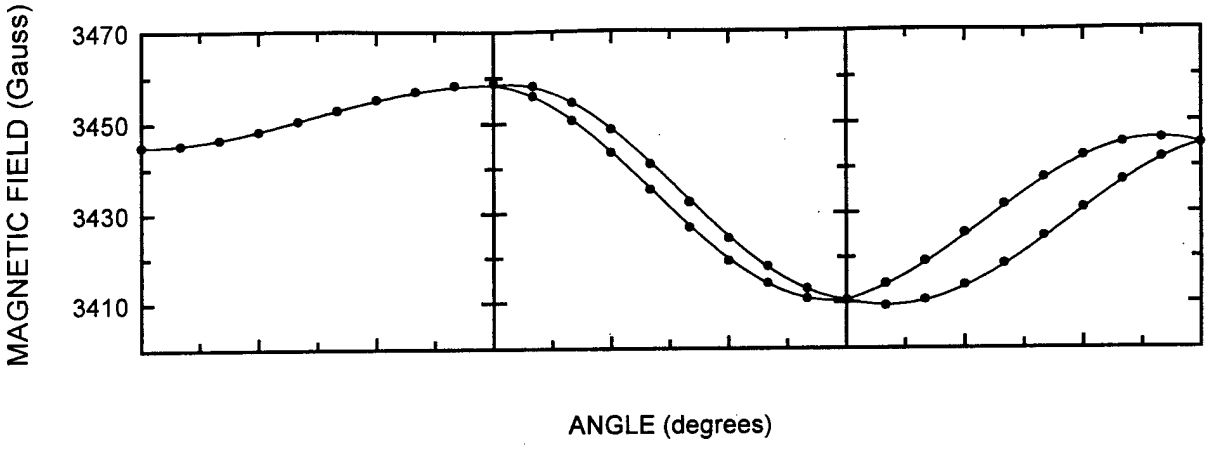


Figure 25. Angular variation of the EPR spectrum of the silicon-associated hole center. The experimental results, obtained at room temperature, are represented by the discrete data points while the solid lines were calculated using the g matrix in Table V.

particular plane. The following S = 1/2 spin-Hamiltonian containing only the electron Zeeman interaction was used to fit the angular dependence data in Figure 25.

$$H = \beta \mathbf{S} \cdot \mathbf{g} \cdot \mathbf{B} \qquad (3)$$

The six parameters needed to describe the g matrix are the three principal values and the three Euler angles specifying the directions of the principal axes. A fitting program involving repeated diagonalization of the 2 x 2 spin-Hamiltonian matrix allowed us to determine the "best" values for these six parameters. The input data for this fitting process consisted of 46 line positions (i.e., magnetic field values) and their associated microwave frequencies taken at 27 angles uniformly distributed over the a-c, b-c, and a-b planes. The resulting best set of parameters for the g matrix are given in Table V for one of the four crystallographically equivalent sites occupied by the silicon-associated hole center. Additional data points were taken at a few angles in the [011] plane to verify the validity of these parameters. Using the symmetry elements of the KTP lattice, one can obtain the g-matrix parameters corresponding to the remaining three sites. Instead of specifying the Euler angles directly in Table V, we have converted them into $(\theta,\phi)$ pairs of angles, thus making it easier to describe the direction of each principal axis. The polar angle $\theta$ is measured relative to the c direction and the azimuthal angle $\phi$ is measured relative to the a direction in the c plane with positive rotation from a to b.

The maximum measured g shift of +0.03 strongly supports the assignment of this holelike center to an $O^-$ ion adjacent to a silicon impurity ion occupying a phosphorus site. Similar hole centers involving $O^-$ ions in other oxide crystals typically have had positive g shifts in the range of 0.02 to 0.08.[53] The four oxygen ions surrounding a phosphorus ion (or in our case, silicon) are crystallographically inequivalent and we can not easily deduce which of the four will trap the hole (i.e., which one will become the $O^-$ ion) because we do not know the orientation of the oxygen p orbital containing the unpaired spin. We have compared the principal axes of the g matrix with the bond directions in the regular KTP lattice, but found no correlation.

TABLE V. Parameters for the room-temperature g matrix of the silicon-associated trapped hole center in KTP. The angles $\theta$ and $\phi$ are defined in the text. Error limits are ±0.0002 for the principal values and ±2° for the angles specifying the principal directions.

| | Principal Directions | |
|---|---|---|
| Principal Values | $\theta$ | $\phi$ |
| 2.0030 | 93.7° | 88.1° |
| 2.0102 | 100.3° | 357.5° |
| 2.0320 | 11.0° | 17.9° |

The silicon-associated trapped hole center in KTP decays slowly over a period of many days at room temperature. Curve (a) in Figure 26 shows a set of decay data taken at room temperature (291 ± 0.5 K). These data were acquired by monitoring the intensity of the hole center's EPR signal for approximately 47 hours following a room-temperature x-ray irradiation. During the first several hundred minutes after the irradiation, the decrease in the intensity of the EPR signal was rapid and data points were taken at 30-minute intervals. As the anneal proceeded to longer times, the rate of decay became much slower and data points were taken less often. Although not shown in Figure 26, the silicon-associated hole signal could still be easily seen two weeks after the beginning of a room-temperature

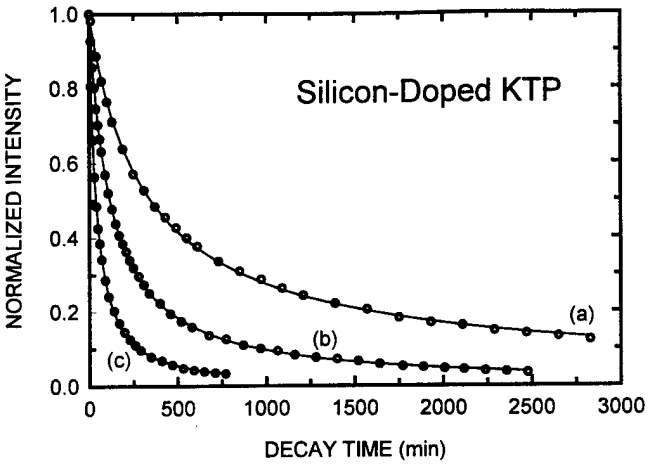


Figure 26. Thermal decay of the silicon-associated hole center. Curves (a), (b), and (c) were taken at 291, 300, and 311 K, respectively. The solid lines represent the best fits to the curves obtained by using Eq. (5).

anneal. Two additional sets of decay data for the silicon-associated hole center were taken at 300 K and 311 K and are shown in curves (b) and (c), respectively, in Figure 26. Much faster decay rates occurred at these higher temperatures. These latter two temperatures were maintained during the anneals by flowing warm nitrogen gas past the sample while it was positioned in the variable-temperature glassware extending through the microwave cavity.

To insure that the curves in Figure 26 could be combined in a single analysis, we subjected the sample to the same radiation dose prior to taking each set of data. The first data point in each of the decay experiments was taken ten minutes after removing the crystal from the x-ray source. During this initial ten-minute period at room temperature, the sample was placed in the EPR cavity and then oriented such that the magnetic field was along the a-axis of the crystal. Once the crystal was suitably aligned, the temperature at which the decay was to be monitored (in the case of the two higher temperature decays) was achieved in less than two minutes. Because the sample was at room temperature for the first ten minutes for all three of the decays illustrated in Figure 26, we have offset the data so that the initial intensity (at $t = 0$ in Figure 26) corresponds to the concentration measured ten minutes after turning off the x-rays.

Before proceeding to an analysis of the decay data, it is helpful to establish which type of charge (trapped electrons or trapped holes) is thermally released during decay and whether more than one type of trap is contributing to the release of charge. In the samples

used in our present investigation, there is a single dominant center representing trapped electrons after a room-temperature irradiation (the $Ti^{3+}$ center labeled Center A) and there are several major centers containing trapped holes (the silicon-associated trapped hole center and the $Fe^{4+}$ and $Cr^{4+}$ ions). These transition-metal ions are not observed with EPR and their presence is deduced by changes in the concentration of the corresponding trivalent ions. When separately monitoring the slow return of the $Fe^{3+}$ and $Cr^{3+}$ EPR signals after an irradiation at room temperature, we observed a time dependence very similar to that shown in curve (a) in Figure 26. This suggests that the decay processes for the various hole centers are controlled by the same mechanism. It thus appears, on the basis of these observations, that the decay process being monitored in our samples is controlled by the release of electrons from the $Ti^{3+}$ traps (i.e., Center A). Since the other three $Ti^{3+}$ traps (Centers B, C, and D in Roelofs' notation) are present at much lower concentrations, we will ignore their contributions to the decay process in the remainder of this analysis.

We initially attempted to fit the three decay curves in Figure 26 using first-order kinetics. These single-exponential solutions did not adequately describe the data, i.e., they were unable to account for the slow rates of decay at the longer anneal times. We then considered second-order kinetics,[54] which takes into account the retrapping of thermally released charges, and found that the fits to the data were greatly improved. However, we obtained the best fit to our thermal decay data when we used a general-order kinetics (GOK) model.[54,55] The GOK model is based on the following differential equation

$$\frac{dn}{dt} = -s' \, n^b \, \exp\left(-E/kT\right) \tag{4}$$

where n is the concentration of electrons that are trapped at a particular time (i.e., the concentration of Center A) and b is a parameter which describes the order of kinetics. Other parameters are the activation energy E, a pre-exponential factor s', and the temperature T. This equation describes first-order kinetics when b equals one, and second-order kinetics when b equals two. The solution to Eq. (4) is

$$n(t) = \frac{n_o}{[a\,t+1]^{\frac{1}{b-1}}} \tag{5}$$

where $n_o$ is the initial concentration of trapped electrons immediately following an irradiation at room temperature (i.e., prior to the beginning of a thermal anneal). In Eq. (5), the parameter a is given by

$$a = s\,(b-1)\,\exp\left(-E/kT\right) \qquad (6)$$

when a "frequency" factor s, with dimensions of $s^{-1}$, is defined in terms of s', $n_o$, and b.

$$s = s'\,n_o^{b-1} \qquad (7)$$

We have used Eq. (5) to separately fit each of the decay curves in Figure 26. The resulting values of the parameters a and b are given below for each anneal temperature.

At 291 K, $a = 0.618 \times 10^{-4}\ s^{-1}$ and $b = 2.19$

At 300 K, $a = 1.22 \times 10^{-4}\ s^{-1}$ and $b = 1.91$

At 311 K, $a = 3.33 \times 10^{-4}\ s^{-1}$ and $b = 1.82$

The parameter b is close to two in each case, which indicates that the kinetics describing the decay processes are primarily second order and that retrapping of charge is an important factor in the decays. We note that b, the order of kinetics, becomes smaller as the temperature increases. After extracting the values of a and b from each decay curve in Figure 26, we proceeded to determine values of the activation energy E and the "frequency" factor s. In general, E and s are expected to be constants for a given thermal-release process and to have very little temperature dependence. Values for E and s were determined by using Eq. (6) to set up a pair of simultaneous equations (i.e., substituting a specific temperature and its corresponding values of a and b into Eq. (6) to obtain one of the equations and then repeating the process with another temperature to obtain the second equation). This procedure of setting up a pair of simultaneous equations was followed for the three combinations of available temperatures and the resulting values of E and s are given below.

For the 291 K/300 K pair: $E = 0.795$ eV and $s = 2.99 \times 10^9\ s^{-1}$

For the 291 K/311 K pair: $E = 0.802$ eV and $s = 4.05 \times 10^9\ s^{-1}$

For the 300 K/311 K pair: $E = 0.809$ eV and $s = 5.20 \times 10^9\ s^{-1}$

The consistency in these results for E and s is encouraging and provides support for our use of general-order kinetics to describe the release of electrons from the $Ti^{3+}$ traps (i.e., Center A) in KTP. Averaging the values for the activation energy and the "frequency" factor gives E = 0.80 eV and $s = 4.1 \times 10^9\ s^{-1}$. An estimate of the error for E is ±0.02 eV and for s is $\pm 2.0 \times 10^9\ s^{-1}$. We note that the ability to directly monitor the sili-

con-associated trapped hole center EPR signal as it decayed was a key factor in our thermal anneal study. The EPR spectrum of many x-ray or laser-induced paramagnetic defects can not be observed at their decay temperatures because of line broadening due to short spin-lattice relaxation times.

## C. $Ti^{3+}$ ELECTRON TRAPS

All of the $Ti^{3+}$ centers presented here can be induced by irradiation either with x-rays or with near-band-edge laser light, though x-irradiation is a more efficient process. The x-ray source was a tube operating at 60 kV and 30 mA with a molybdenum target. For x-irradiation at low temperature, the KTP samples were held in a liquid-nitrogen-filled styrofoam cup placed directly in front of the tube window. Room-temperature irradiation was performed in the same manner, except the cup was either empty or filled with ice water to minimize heating. For laser irradiation, near-band-edge light was obtained with the 355-nm third harmonic (the band edge of KTP is ~350 nm at room temperature) of a pulsed Continuum Powerlite Nd:YAG laser operating at 10-Hz repetition rate. The laser pulse width was approximately 6 ns and the average third-harmonic power was around 1 W. Dichroic mirrors diverted the fundamental and second-harmonic beams so that only the 355-nm light was incident on the crystal. For room temperature laser irradiation, the samples were mounted directly in the path of the laser beam. For low temperature studies, samples were held in a liquid-nitrogen-filled quartz finger dewar. After low temperature irradiation, samples were transferred without warming into the pre-cooled optical or EPR cryostat for measurements.

Our EPR and ENDOR studies were performed on a Bruker Instruments ESP-300 spectrometer operating near 9.5 GHz. A rectangular $TE_{102}$ cavity was used for most EPR measurements while a cylindrical $TE_{011}$ cavity was used for ENDOR experiments. The final EPR and ENDOR angular dependence data were taken at the same time in the cylindrical cavity. A piece of flexible waveguide and a custom-design tilt control allow the cavity to be adjusted within the magnet gap. This is useful for aligning the crystal with respect to the magnetic field. Both cavities were fit with Oxford Instruments gas-flow cryostats allowing controllable sample temperatures in the range from 8 to 300 K. For EPR measurements, the magnetic field was amplitude modulated at 100 kHz in the rectangular cavity and 25 kHz in the cylindrical cavity. The rf field used for ENDOR measurements was frequency modulated at 12.5 kHz. The applied magnetic field was measured with a Varian E-500 digital gaussmeter while the microwave frequency was measured with either a Hewlett-Packard 5340A or 5352B counter. The small difference in magnetic field be-

tween the gaussmeter and the sample position (~1.5 G) was corrected by measuring the resonance of Cr:MgO. The isotropic g value of $Cr^{3+}$ in MgO is well known (g = 1.9800). The cryostat glassware limited the sample dimensions to no larger than 3 x 3 x 6 $mm^3$. Unless otherwise noted, Litton Airtron (Charlotte, NC), provided all hydrothermal-grown samples and Crystal Associates (East Hanover, NJ), provided the flux-grown samples.

Determination of the g and A matrices for the different $Ti^{3+}$ centers required measurement of the angular dependence of the EPR and ENDOR lines. Since KTP crystals are typically free of random strain, the resonance lines are relatively narrow. In addition, the low symmetry of the lattice results in a strong angular dependence. These aspects make alignment of the magnetic field in any crystal plane or along any axis certain, albeit difficult. For the angular dependence study, crystals were mounted in a teflon holder and secured in the microwave cavity. Adjustments to the cavity were made to insure that the field would not stray from a crystallographic plane as the magnet was rotated. This was confirmed by observing the EPR spectrum and checking that the signal did not split into more than two components as the magnet was turned.

The EPR angular dependence data for each center were fit by least squares analysis to the general electron-Zeeman spin-Hamiltonian (see Eq. (3)). The principal values and principal-axis directions were initally chosen arbitrarily. A least-squares analysis program written for Matlab iteratively determined the set of six parameters (three g values and three Euler angles) that best describe the actual angular dependence. To facilitate data analysis, the Euler angles have been decomposed into polar coordinates with respect to the crystal axes. The direction of each principal axis is then described by a pair of angles $\theta$ and $\varphi$. The polar angle ($\theta$) is measured from the $+c$ direction and the azimuthal angle ($\varphi$) is measured in the $c$ plane from the $a$ axis towards the $b$ axis.

Since the low-frequency region of the ENDOR spectrum was often quite noisy and poorly resolved, only the high-frequency ENDOR line (recall ENDOR lines always occur in pairs) was used to find the A matrix of each interaction. The appropriate spin-Hamiltonian for the analysis of the ENDOR data is

$$\hat{\mathbf{H}} = \beta \hat{\mathbf{S}} \cdot \mathbf{g} \cdot \mathbf{H} + \hat{\mathbf{I}} \cdot \mathbf{A} \cdot \hat{\mathbf{S}} - \mathbf{g}_N \beta_N \mathbf{H} \cdot \hat{\mathbf{I}} \qquad (8)$$

Of the five $Ti^{3+}$ centers described in this section, two are present in flux-grown material, denoted $A_{flx}$ and $I_{flx}$, and three are present in hydrothermal-grown material, denoted $I_{hyd}$, $II_{hyd}$, and $III_{hyd}$. A convention has been adopted whereby a center identified

with a letter is stable at room temperature while a center identified with a numeral is stable only at lower temperatures. The subscript then indicates the type of material the center is present in (i.e., flx = flux, hyd = hydrothermal). $III_{hyd}$ is an order of magnitude smaller than $I_{hyd}$ and $II_{hyd}$ and no ENDOR data were available for analysis of the hyperfine structure. This center has never been reported in the literature, although the other four centers have. Prior reports on titanium centers in KTP, however, lacked complete characterization and defect models were limited.

Figures 27 through 31 show EPR spectra of the $Ti^{3+}$ centers along the crystallographic directions that reveal the most hyperfine structure. All EPR spectra were taken with the microwave frequency near 9.49 GHz. The horizontal axis for each spectrum has been corrected to account for the difference between the magnetic field as measured by the spectrometer Hall probe and that measured by the gaussmeter. For the four largest centers, an ENDOR spectrum revealing the dominant interactions is associated with each EPR spectrum. Temperature settings for all spectra are included in the text along with the discussion of each center. Figures 32 through 40 contain angular dependence plots that will be referred to throughout the discussion.

The first $Ti^{3+}$ center analyzed is denoted $I_{flx}$. It is formed in flux-grown material during an irradiation at 77 K and decays away quickly at temperatures above ~200 K. Scripsick et al.[38] briefly reported EPR and ENDOR results on this center, although it was then mistakenly identified as Roelofs'[27] center B and no spin-Hamiltonian parameters were determined. The EPR spectrum taken with the field along the *a* axis (shown in Figure 27(a)) indicates an interaction with three 100% abundant I = 1/2 nuclei.

When the field is aligned along the crystal axes, the effective g values of the fourfold degenerate lines are $g_a = 1.8940$, $g_b = 1.8614$, and $g_c = 1.6939$. The EPR linewidth ($\Delta H$) is typically about 1.4 G, although the lines become strikingly broad ($\Delta H \sim 8$ G) along the *c* axis. The ENDOR linewidth was ~50 kHz. Unless otherwise noted, all linewidths are measured as peak-to-peak width in both EPR and ENDOR spectra and not according to any assumption regarding Gaussian or Lorentzian lineshapes. The optimum temperature for observation of the EPR spectrum was ~25 K while the best temperature for measuring the ENDOR spectrum was ~10 K. Figure 27(b) is the ENDOR spectrum acquired monitoring the middle line of the *a* axis EPR spectrum. A large line at 6.188 MHz is the "free spin" line of phosphorus. This line arises when there is a large number of very weak phosphorus interactions. Consequently, there are many lines centered at $\nu_N$ with negligible A values, causing an overlap. Stick diagrams in the figure indicate important pairs of lines.

There are two pairs of lines separated by twice $\nu_N$ for $^{31}P$ (indicating $\nu_N < A/2$), and one pair centered on $\nu_N$ for $^{31}P$ (indicating $\nu_N > A/2$). A fourth, weaker interaction is also centered on $\nu_N$ but this was unresolved at many orientations and was not followed in the angular dependence. No lines could be attributed to an interaction with a proton ($^1H$).

Table VI summarizes the EPR and ENDOR parameters of center $I_{flx}$, as determined by least-squares analysis. The principal values and $\theta,\varphi$ polar angles corresponding to the principal axes directions are given for each matrix. The table also includes the number of data points used to determine the parameters and the root-mean-square deviation $\langle dev \rangle$ between measured and calculated line positions. The three principal g values are all unique, consistent with the low symmetry of the defect site, while the hyperfine matrices are all axial, consistent with the dipole-dipole nature of the interaction. By convention, the axis with the largest principal value is identified as the z axis.

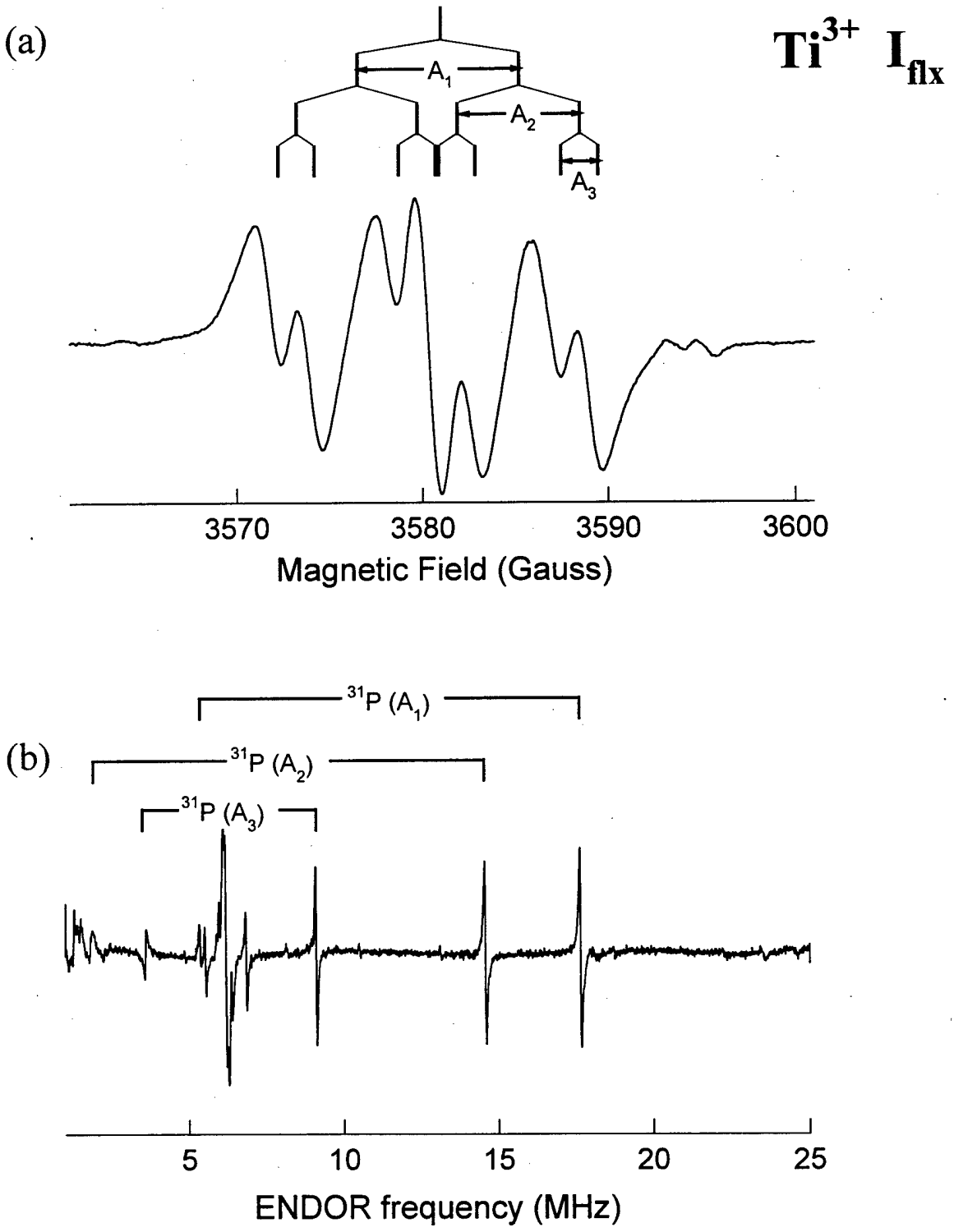


Figure 27. (a) EPR and (b) ENDOR spectra of $Ti^{3+}$ center $I_{flx}$ in flux-grown KTP taken with H || a. The stick diagram in (a) shows splitting due to three 100% abundant I = 1/2 nuclei. The ENDOR spectrum reveals all three nuclei are phosphorus ($^{31}P$).

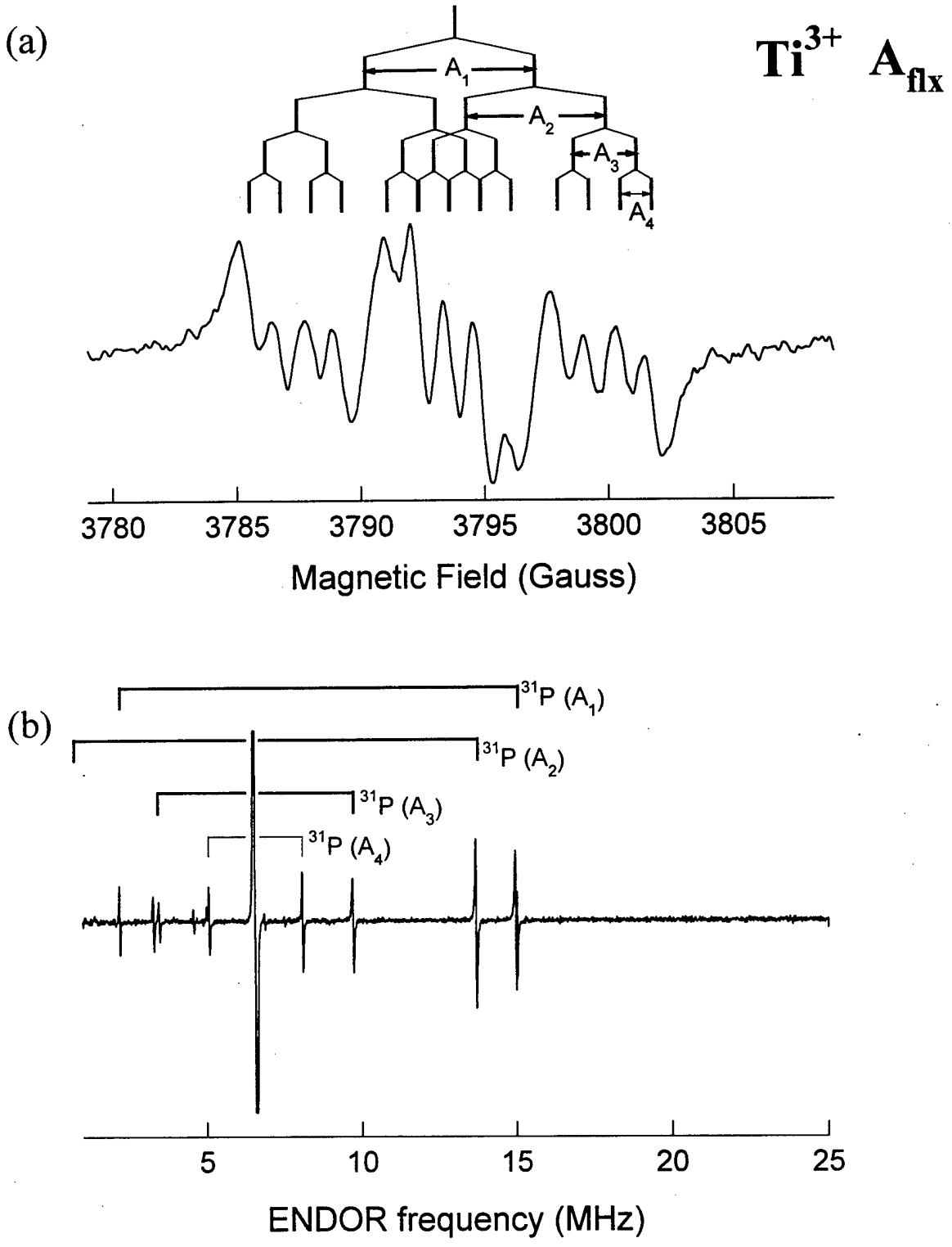


Figure 28. (a) EPR and (b) ENDOR spectra of $Ti^{3+}$ center $A_{flx}$ in flux-grown KTP taken with H || c. The stick diagram in (a) shows splitting due to four 100% abundant I = 1/2 nuclei. The ENDOR spectrum reveals that all four nuclei are phosphorus ($^{31}P$).

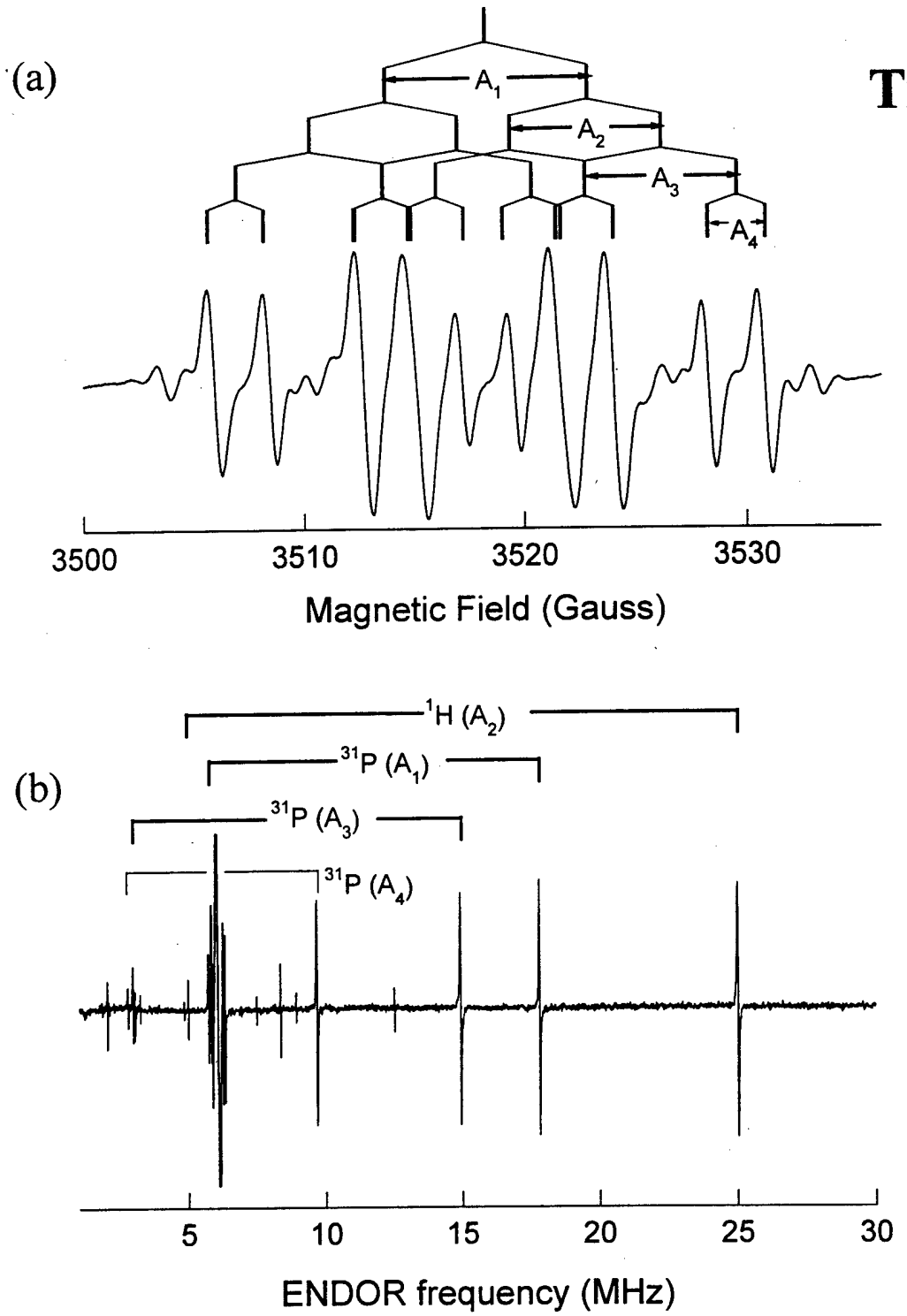


Figure 29. (a) EPR and (b) ENDOR spectra of $Ti^{3+}$ center $I_{hyd}$ in hydrothermal-grown KTP taken with H || a. The stick diagram in (a) shows splitting due to four 100% abundant I = 1/2 nuclei. The ENDOR spectra reveals three nuclei are phosphorus ($^{31}P$) and one is a proton ($^1H$).

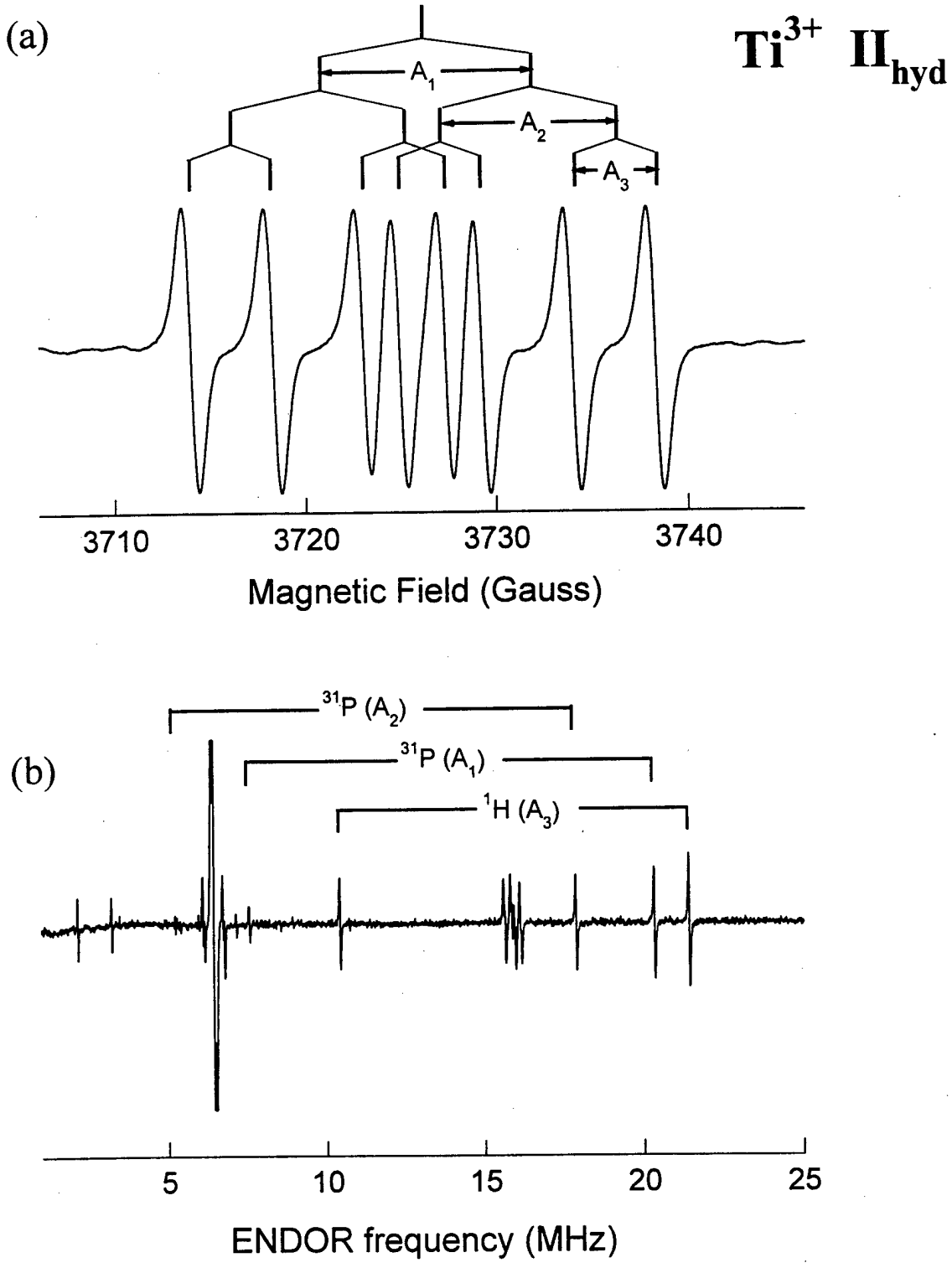


Figure 30. (a) EPR and (b) ENDOR spectra of $Ti^{3+}$ center $II_{hyd}$ in hydrothermal-grown KTP taken with H || a. The stick diagram in (a) shows splitting due to three 100% abundant I = 1/2 nuclei. The ENDOR spectra reveals two nuclei are phosphorus ($^{31}P$) and one is a proton ($^{1}H$).

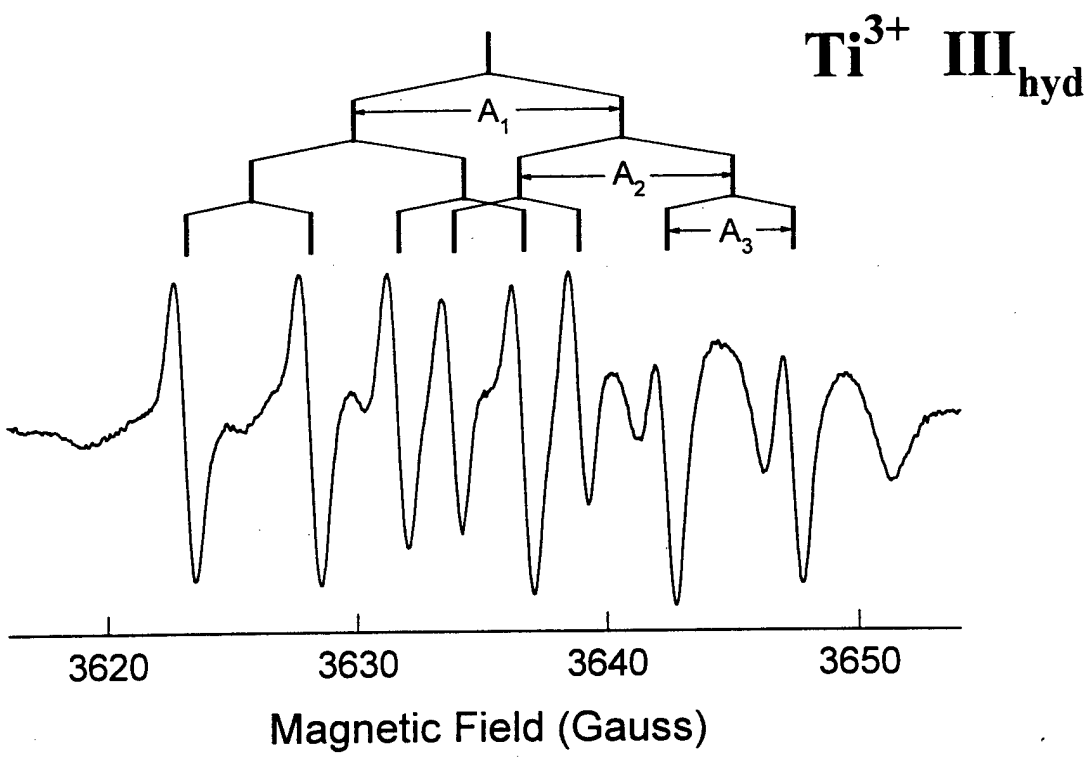


Figure 31. EPR spectrum of $Ti^{3+}$ center $III_{hyd}$ in hydrothermal-grown KTP taken with H || a. The stick diagram shows splitting due to three 100% abundant I = 1/2 nuclei.

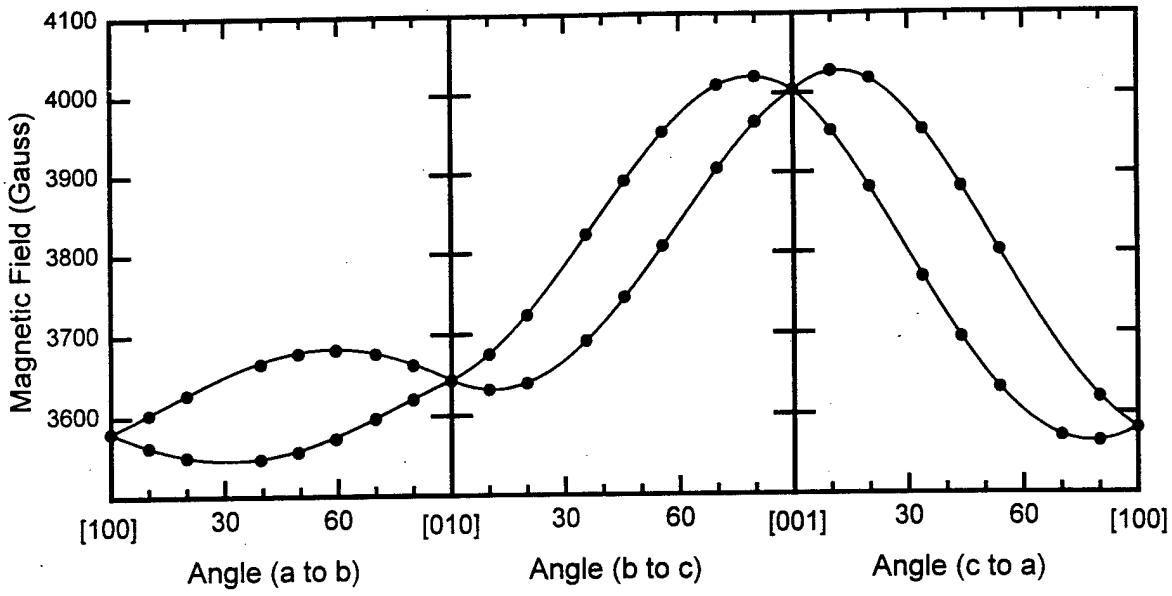


Figure 32. Angular dependence of $I_{flx}$ EPR spectrum. Circles represent experimental values while the lines are generated using best-fit parameters from the spin-Hamiltonian analysis.

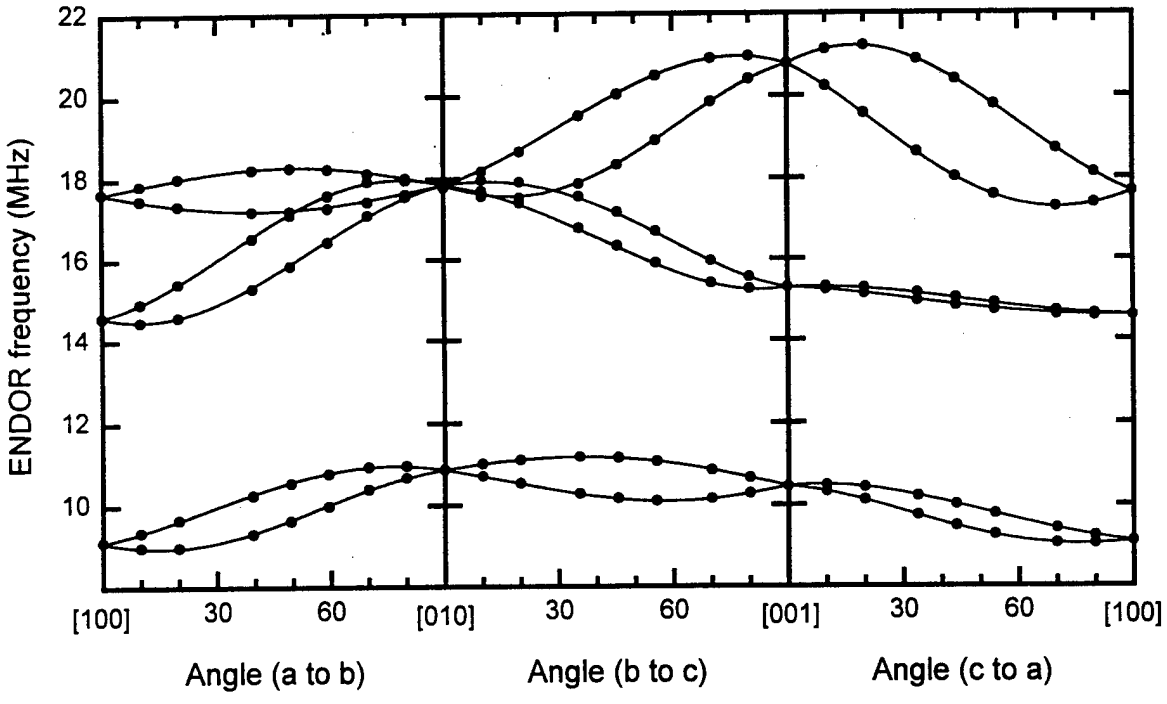


Figure 33. Angular dependence of $I_{flx}$ ENDOR spectra. Circles represent experimental values while the lines are generated using best-fit parameters from the spin-Hamiltonian analysis.

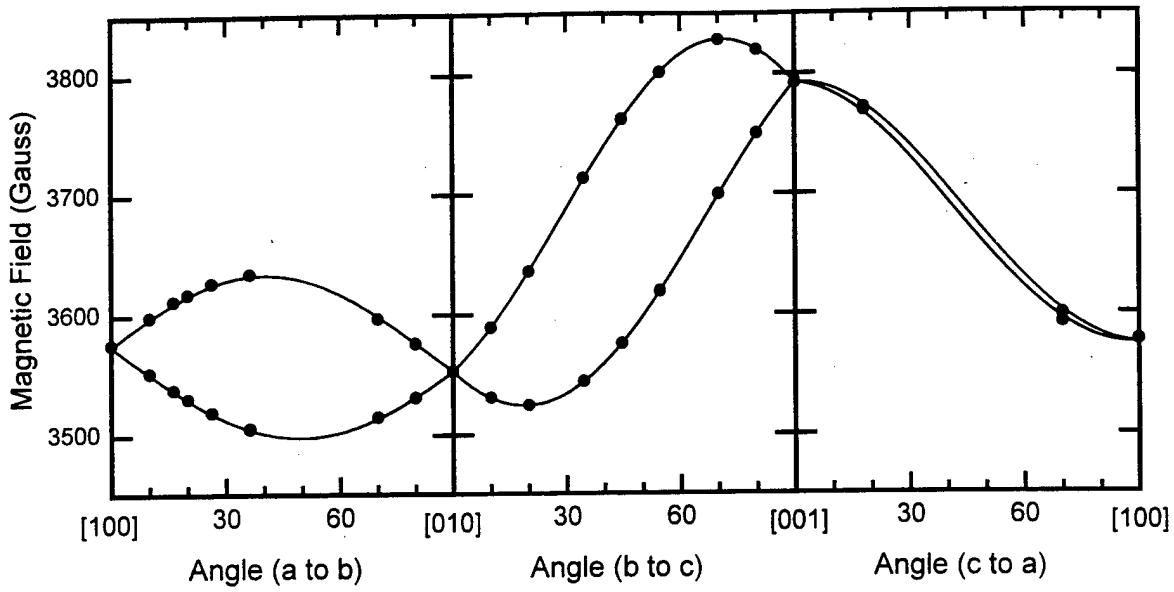


Figure 34. Angular dependence of $A_{flx}$ EPR spectrum. Circles represent experimental values while the lines are generated using best-fit parameters from the spin-Hamiltonian analysis.

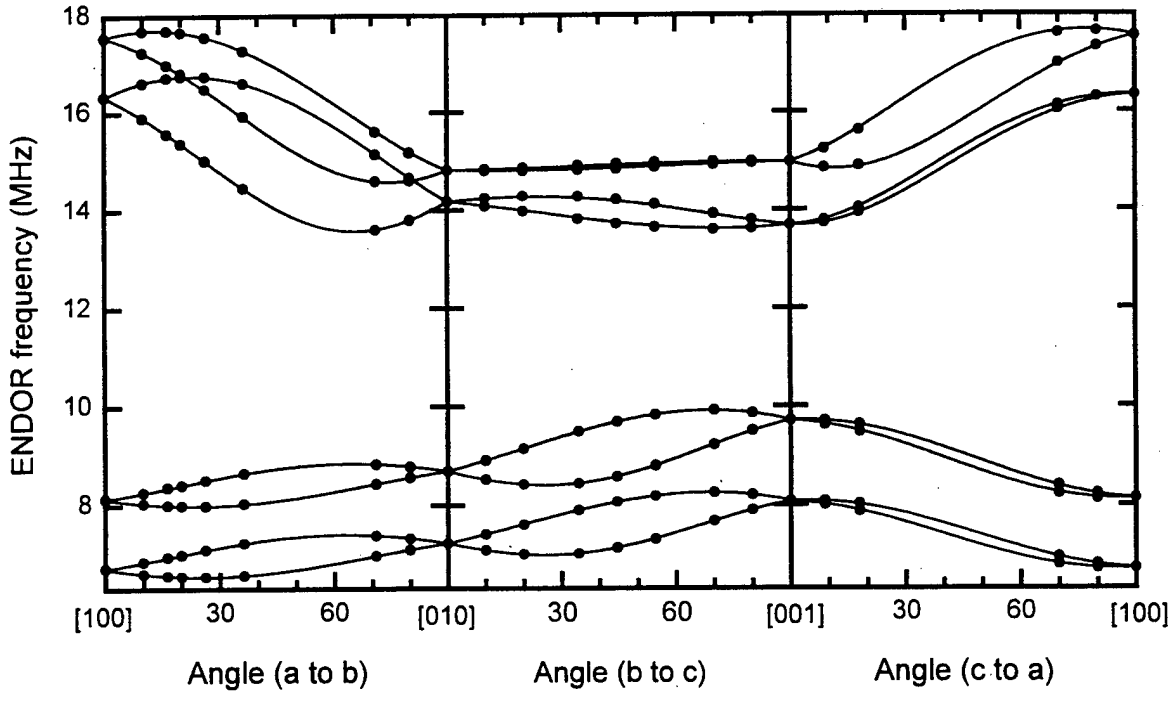


Figure 35. Angular dependence of $A_{flx}$ ENDOR spectra. Circles represent experimental values while the lines are generated using best-fit parameters from the spin-Hamiltonian analysis.

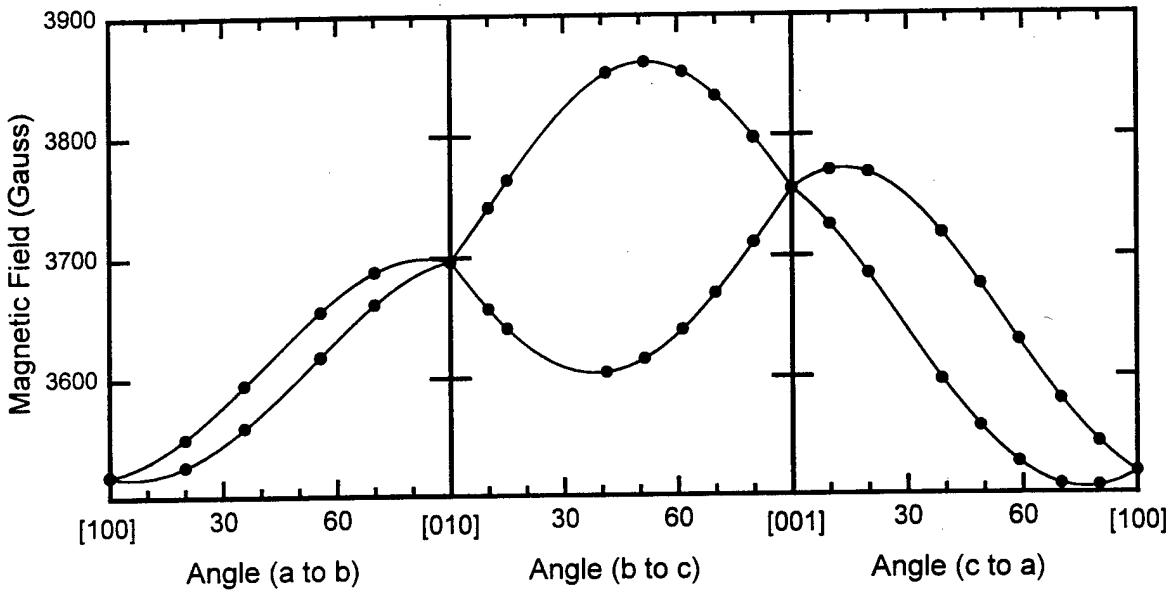


Figure 36. Angular dependence of $I_{hyd}$ EPR spectrum. Circles represent experimental values while the lines are generated usig best-fit parameters from the spin-Hamiltonian analysis.

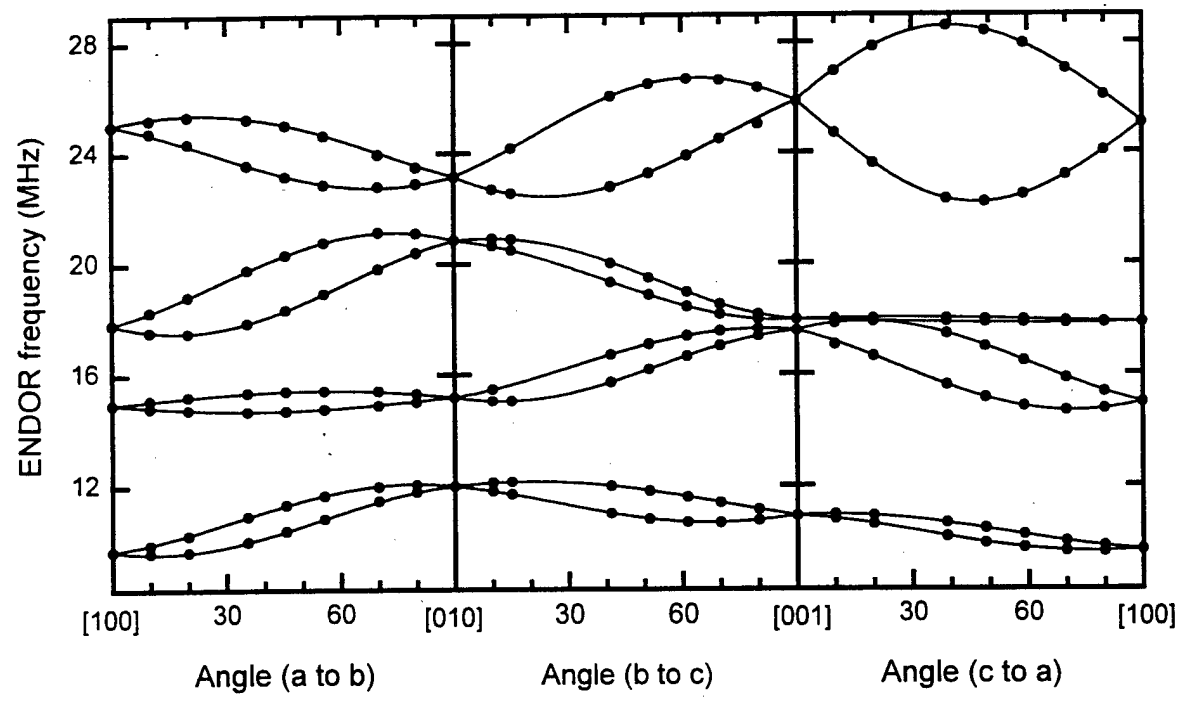


Figure 37. Angular dependence of $I_{hyd}$ ENDOR spectra. Circles represent experimental values while the lines are generated usig best-fit parameters from the spin-Hamiltonian analysis.

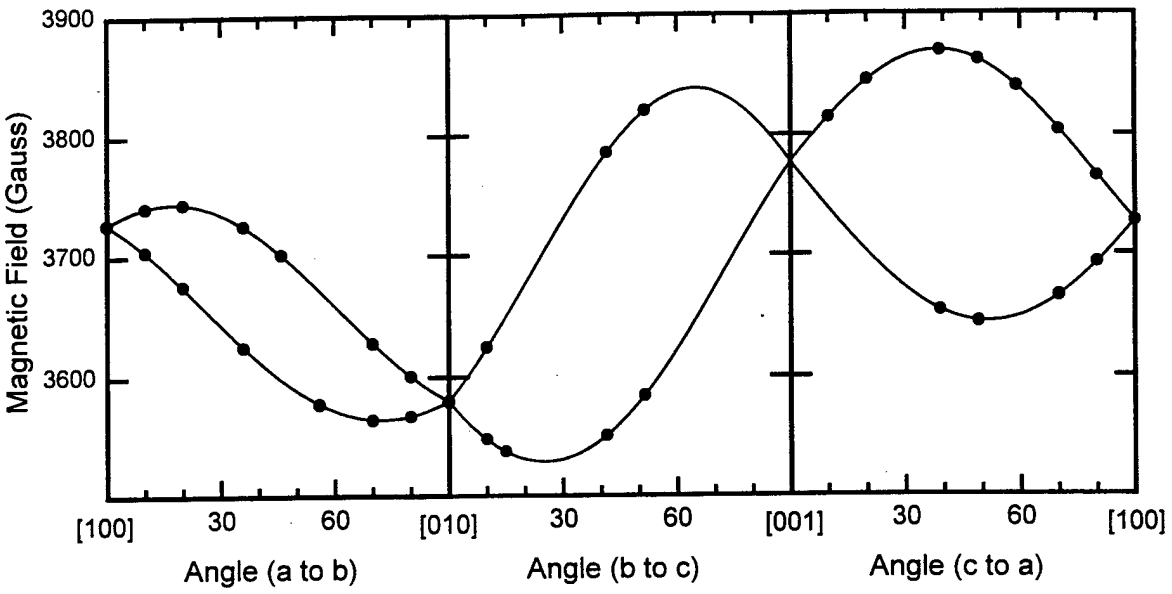


Figure 38. Angular dependence of $II_{hyd}$ EPR spectrum. Circles represent experimental values while the lines are generated using best-fit parameters from the spin-Hamiltonian analysis.

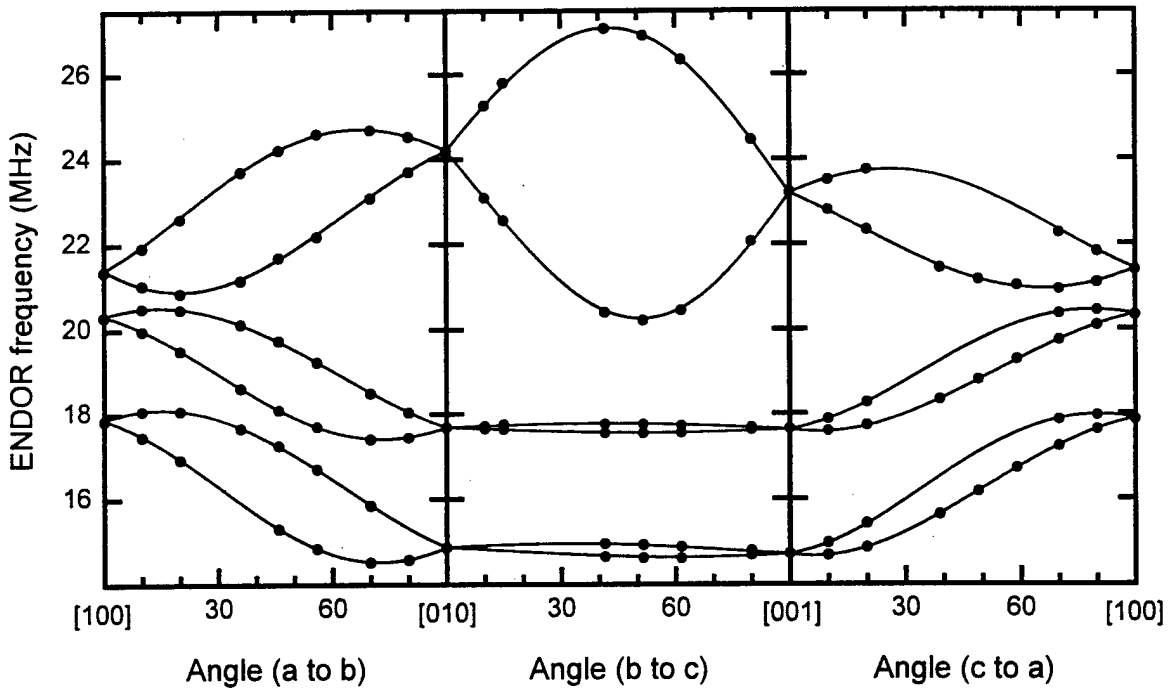


Figure 39. Angular dependence of $II_{hyd}$ ENDOR spectra. Circles represent experimental values while the lines are generated using best-fit parameters from the spin-Hamiltonian analysis.

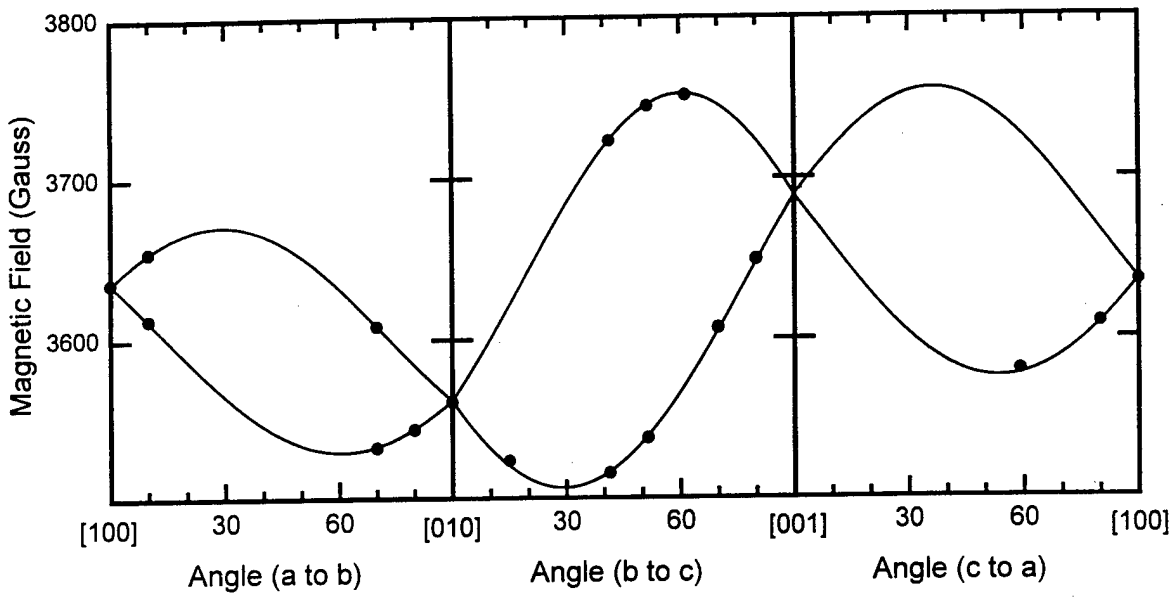


Figure 40. Angular dependence of $III_{hyd}$ EPR spectrum. Circles represent experimental values while the lines are generated using best-fit parameters from the spin-Hamiltonian analysis.

It is worth noting that the θ,φ values listed here are the principal-axis directions at site #1, a designation that has been made arbitrarily. When the EPR spectrum is split into two components in the crystal planes, site #1 is defined as that which gives high field resonance in the *c* plane, high field resonance in the *a* plane, and low field resonance in the *b* plane. As noted before, there are three other ways to assign site #1 and still obtain physically meaningful results. These three ways result in the same principal values, though the principal axes are in terms of another crystallographic site.

| | | Principal Value | | | # of Points | <dev> |
|---|---|---|---|---|---|---|
| | $g_x$ | 1.67961 | 13.5 | 140.2 | | |
| g | $g_y$ | 1.84208 | 91.7 | 57.3 | 53 | 0.22 G |
| | $g_z$ | 1.92526 | 76.6 | 327.8 | | |
| | | | | | | |
| | $A_x$ | 22.12 | 95.2 | 304.0 | | |
| $^{31}$P #1 | $A_y$ | 22.24 | 62.9 | 31.3 | 54 | 4.7 kHz |
| | $A_z$ | 29.15 | 27.7 | 224.0 | | |
| | | | | | | |
| | $A_x$ | 16.61 | 73.7 | 172.2 | | |
| $^{31}$P #2 | $A_y$ | 16.74 | 17.1 | 334.4 | 54 | 5.1 kHz |
| | $A_z$ | 23.45 | 95.0 | 260.8 | | |
| | | | | | | |
| | $A_x$ | 5.292 | 72.2 | 190.7 | | |
| $^{31}$P #3 | $A_y$ | 6.488 | 149.0 | 248.5 | 54 | 2.1 kHz |
| | $A_z$ | 10.04 | 65.5 | 289.2 | | |

Table VI. Principal values and directions of the g and A matrices for the $I_{flx}$ $Ti^{3+}$ center in flux grown KTP. Angles are in degrees and hyperfine parameters are in MHz.

Figure 32 is the angular dependence of the EPR spectrum, with data represented by solid circles and the calculated curves using parameters determined by the least squares analysis. Similarly, Figure 33 is the angular dependence of the ENDOR spectra.

The next $Ti^{3+}$ center analyzed is easily created in flux material by irradiation at room temperature. It is present after 77 K irradiation, though the EPR spectrum is very weak. The intensity will increase as the sample is warmed above ~200 K, indicating that it traps the electrons released by $I_{flx}$. Although it is considered "stable" at 300 K, it slowly anneals out over a period of several days at that temperature. Roelofs[27] first reported it as

center A, and to be consistent with his notation while still distinguishing centers seen in flux-grown and hydrothermal-grown material, it is called $A_{flx}$. During the present study, it has only been seen in flux-grown material although Roelofs claims it can be produced by reduction of hydrothermal-grown material.

Figure 28 shows the EPR and ENDOR spectra of this center taken with the magnetic field along the *c* axis. The effective g values of this center measured along the crystal axes are $g_a = 1.8962$, $g_b = 1.9085$, and $g_c = 1.7882$. EPR measurements were performed around 30 K and ENDOR measurements were made at 13 K. The EPR linewidth was typically ~0.75 G and the ENDOR linewidth was ~50 kHz. The EPR spectrum of Fig. 28(a) reveals four 100% abundant I = 1/2 hyperfine interactions, as shown by the stick diagram. The ENDOR spectrum confirms that all of these interactions are with $^{31}P$ nuclei. Two interactions are of the type $\nu_N < A/2$, with lines separated by twice $\nu_N$ of $^{31}P$. The two weaker interactions are centered on $\nu_N$ for $^{31}P$. All smaller lines in this spectrum can be explained as harmonics of other lines in the spectrum.

| | | **principal value** | | | **# of points** | **<dev>** |
|---|---|---|---|---|---|---|
| | $g_x$ | 1.77040 | 20.7 | 75.9 | | |
| g | $g_y$ | 1.87344 | 74.9 | 211.6 | 44 | 0.74 G |
| | $g_z$ | 1.94725 | 76.2 | 305.4 | | |
| | | | | | | |
| | $A_x$ | 16.58 | 10.5 | 160.5 | | |
| $^{31}P$ #1 | $A_y$ | 16.75 | 89.4 | 253.9 | 48 | 10.2 kHz |
| | $A_z$ | 23.36 | 100.4 | 164.0 | | |
| | | | | | | |
| | $A_x$ | 14.28 | 2.0 | 335.9 | | |
| $^{31}P$ #2 | $A_y$ | 14.68 | 90.0 | 244.8 | 48 | 14.6 kHz |
| | $A_z$ | 21.37 | 88.0 | 154.8 | | |
| | | | | | | |
| | $A_x$ | 3.735 | 76.6 | 147.8 | | |
| $^{31}P$ #3 | $A_y$ | 4.240 | 121.2 | 229.6 | 48 | 2.2 kHz |
| | $A_z$ | 7.229 | 34.5 | 258.1 | | |
| | | | | | | |
| | $A_x$ | 0.844 | 76.0 | 146.8 | | |
| $^{31}P$ #4 | $A_y$ | 1.397 | 56.8 | 47.4 | 48 | 3.2 kHz |
| | $A_z$ | 3.937 | 36.8 | 256.4 | | |

Table VII. Principal values and directions of the g and A matrices for the $A_{flx}$ $Ti^{3+}$ center in flux grown KTP. Angles are in degrees and hyperfine parameters are in MHz.

The circles in figures 34 and 35 show the experimental angular dependence of the EPR and ENDOR spectra, respectively. The lines are generated using parameters listed in Table IV, which are determined by a least-squares analysis of the data.

The $Ti^{3+}$ centers induced in hydrothermal-grown KTP also reveal considerable hyperfine structure. Center $I_{hyd}$ is formed when the sample is irradiated at low temperatures and will anneal out above ~150 K. For this center, the g values along the crystal axes are $g_a = 1.9245$, $g_b = 1.8321$, and $g_c = 1.8034$. The EPR spectrum was optimized around 30 K while the ENDOR spectrum was best observed at 10 K. The EPR linewidth was typically ~0.70 G and the ENDOR linewidth was ~45 kHz.

Figure 29 shows the EPR and ENDOR spectra of this center taken with the magnetic field along the *a* axis. The EPR spectrum shows four 100% abundant I = ½ hyperfine interactions, and the ENDOR spectrum reveals that three of these interactions are with $^{31}P$ nuclei while one is with a proton ($^{1}H$). Two phosphorus interactions give pairs of lines separated by twice $\nu_N$ of $^{31}P$ while the third phosphorus interaction yields lines centered on $\nu_N$ of $^{31}P$. The fourth I = ½ interaction gives lines centered on $\nu_N$ for $^{1}H$.

| | | principal | | | # of | |
|---|---|---|---|---|---|---|
| | | value | θ | ϕ | Points | <dev> |
| | $g_x$ | 1.75206 | 37.5 | 100.2 | | |
| g | $g_y$ | 1.86722 | 59.0 | 241.9 | 48 | 0.29 G |
| | $g_z$ | 1.93830 | 108.9 | 163.7 | | |
| | | | | | | |
| | $A_x$ | 13.87 | 44.0 | 323.2 | | |
| $^{1}H$ | $A_y$ | 14.09 | 98.6 | 242.1 | 53 | 9.5 kHz |
| | $A_z$ | 26.37 | 47.3 | 160.1 | | |
| | | | | | | |
| | $A_x$ | 22.84 | 9.7 | 329.0 | | |
| $^{31}P$ #1 | $A_y$ | 22.94 | 80.6 | 162.6 | 54 | 11.3 kHz |
| | $A_z$ | 29.54 | 92.2 | 252.3 | | |
| | | | | | | |
| | $A_x$ | 17.010 | 94.2 | 300.3 | | |
| $^{31}P$ #2 | $A_y$ | 17.217 | 66.3 | 28.5 | 53 | 4.7 kHz |
| | $A_z$ | 23.051 | 24.1 | 219.8 | | |
| | | | | | | |
| | $A_x$ | 6.888 | 77.0 | 188.4 | | |
| $^{31}P$ #3 | $A_y$ | 8.102 | 28.5 | 73.3 | 54 | 4.1 kHz |
| | $A_z$ | 12.030 | 65.1 | 284.5 | | |

Table VIII. Principal values and directions of the g and A matrices for the $I_{hyd}$ $Ti^{3+}$ center in hydrothermal grown KTP. Angles are in degrees and hyperfine parameters are in MHz.

The circles in figs. 36 and 37 show the angular dependence of the EPR and ENDOR spectra, respectively. The lines are generated using parameters listed in Table VIII, which have been determined by a least-squares analysis of the angular dependence data.

The other dominant $Ti^{3+}$ center in hydrothermal-grown KTP is denoted $II_{hyd}$. Like $I_{hyd}$, it is formed when the sample is irradiated at low temperatures and will anneal out above ~150 K. The g values along the crystal axes are $g_a = 1.8172$, and $g_b = 1.8916$. The value of $g_c$ was not directly measurable due to an overlap of EPR signals, but the spin Hamiltonian parameters predict $g_c = 1.7931$. The EPR spectrum was optimized around 30 K while the ENDOR spectrum was best observed at 10 K. The EPR linewidth was typically ~0.75 G and the ENDOR linewidth was ~50 kHz.

Figure 30 shows the EPR and ENDOR spectra of this center taken with the magnetic field along the *a* axis. The EPR spectrum reveals hyperfine interaction with three 100% abundant I = ½ nuclei and the ENDOR spectrum shows that two of these interactions are with phosphorus nuclei while one is with a proton. Both of the interactions that are attributable to phosphorus are separated by twice $\nu_N$ for $^{31}P$. The third, weakest interaction gives a pair of ENDOR lines centered at $\nu_N$ for $^{1}H$.

| | | principal | | | # of | |
|---|---|---|---|---|---|---|
| | | value | θ | ϕ | points | <dev> |
| | $g_x$ | 1.72439 | 40.8 | 33.6 | | |
| g | $g_y$ | 1.85489 | 59.8 | 165.8 | 38 | 0.31 G |
| | $g_z$ | 1.91876 | 114.7 | 91.4 | | |
| | | | | | | |
| | $A_x$ | 9.76 | 133.7 | 122.8 | | |
| $^{1}H$ | $A_y$ | 10.71 | 63.9 | 184.9 | 49 | 7.1 kHz |
| | $A_z$ | 22.61 | 125.0 | 254.9 | | |
| | | | | | | |
| | $A_x$ | 22.15 | 19.7 | 86.4 | | |
| $^{31}P$ #1 | $A_y$ | 22.32 | 108.9 | 70.1 | 49 | 7.8 kHz |
| | $A_z$ | 28.38 | 95.1 | 161.8 | | |
| | | | | | | |
| | $A_x$ | 16.36 | 4.8 | 130.5 | | |
| $^{31}P$ #2 | $A_y$ | 16.53 | 92.5 | 71.3 | 43 | 9.0 kHz |
| | $A_z$ | 23.54 | 94.1 | 161.5 | | |

Table IX. Principal values and directions of the g and A matrices for the $II_{hyd}$ $Ti^{3+}$ center in hydrothermal grown KTP. Angles are in degrees and hyperfine parameters are in MHz.

Circles in figures 38 and 39 represent the experimental data and show the EPR and ENDOR angular dependence, respectively. The lines are generated using spin-Hamiltonian parameters determined by a least-squares analysis of this data, as summarized in Table IX.

The last hydrothermal $Ti^{3+}$ center analyzed is denoted $III_{hyd}$. It has the same formation and decay behavior as $I_{hyd}$ and $II_{hyd}$. It is an order of magnitude less intense than the other centers but has been included because it exhibits some curious properties. The g values along the crystal axes are $g_a = 1.8627$, and $g_b = 1.9011$. The value of $g_c$ was not directly measurable due to an overlap of EPR signals, but the spin Hamiltonian parameters yield $g_c = 1.8356$. The EPR spectrum was optimized around 30 K and the linewidth was typically ~0.75 G.

Figure 31 shows the EPR spectrum of this center taken with the magnetic field along the *a* axis and reveals hyperfine interactions with three 100% abundant I = ½ nuclei, strikingly similar to the spectrum for $II_{hyd}$. The identity of the neighboring nuclei can not be verified since there is no ENDOR data for this center. Circles in figure 40 represent the experimental angular dependence data and the lines are generated using spin-Hamiltonian parameters determined by least-squares analysis. These parameters are summarized in Table X. There is a remarkable similarity between $II_{hyd}$ and $III_{hyd}$, especially when one considers the low symmetry of the material. This similarity is directly reflected in the principal-axis directions.

| | | Principal | | | # of | |
|---|---|---|---|---|---|---|
| | | Value | θ | ϕ | points | <dev> |
| | $g_x$ | 1.77158 | 42.5 | 40.6 | | |
| g | $g_y$ | 1.89305 | 58.9 | 171.7 | 21 | 0.29 G |
| | $g_z$ | 1.93153 | 115.9 | 98.7 | | |

Table X. Principal values and directions of the g matrix for the $III_{hyd}$ $Ti^{3+}$ center in hydrothermal grown KTP. Angles are in degrees.

The results of these studies of $Ti^{3+}$ electron traps are summarized in the PhD dissertation of Scott Setzler.[51] His summary and conclusions follow. Electron paramagnetic resonance and electron-nuclear double resonance experiments have been performed on radiation-induced titanium electron traps in KTP. Three of these centers are only present in hydrothermal-grown KTP ($I_{hyd}$, $II_{hyd}$, and $III_{hyd}$) and the others are only present in flux-

grown KTP ($I_{flx}$ and $A_{flx}$). The g matrices of all five centers have been determined by analysis of the angular dependence of the EPR lines. Each center displays considerable hyperfine interactions with neighboring phosphorus ions while the centers in hydrothermal KTP also exhibit an interaction with a proton. An analysis of the angular dependence of ENDOR lines provided the A matrices describing the hyperfine interactions, which in turn has allowed the centers to be identified according to which crystallographically unique titanium ion traps the electron.

Further consideration has provided reasonable explanations for the observed defect stability. The flux centers represent electrons trapped at each unique titanium ion. The $I_{flx}$ center, trapped at Ti(1), is stabilized by a nearby divalent impurity and is only stable below ~200 K, while the $A_{flx}$ center, trapped at Ti(2), is stabilized by an adjacent oxygen vacancy. Divalent impurities and oxygen vacancies are required to charge compensate the large number of potassium vacancies present in flux material. The hydrothermal centers are all stabilized by nearby protons. These protons appear to be the only significant charge compensation present in hydrothermal material studied here.

The low thermal stability of $Ti^{3+}$ centers in hydrothermal KTP is consistent with the belief that this material is more resistant to gray-track damage, but high rep-rate applications may still be affected by the short lived $I_{hyd}$ and $II_{hyd}$ centers. Elimination of impurities from flux material should improve device performance. Although the oxygen vacancy-related electron trap is stable at room temperature, it is the existence of impurity-related hole traps ($Si^{4+}$ and $Fe^{2+}$) that give rise to an extended defect lifetime. If these impurities are not present, no stable hole centers will form and the electrons will recombine before forming an $A_{flx}$ center. High repetition-rate applications may still suffer, just as with hydrothermal material, since there are still some "native" defects related only to stoichiometry.

Elimination of point defects during growth is the ideal solution to the suppression of gray tracks, but it is also the most difficult. In fact, elimination of impurities is not nearly as simple as it may sound, since they are intricately linked to the presence of native defects. It is still unresolved whether impurities are incorporated into the crystal to charge compensate vacancies, or vacancies form to compensate impurities. It is undeniable, however, that ultimate device performance will be achieved when the presence of point defects is minimized.

## REFERENCES


1. P. G. Schunemann, P. J. Drevinsky, M. C. Ohmer, W. C. Mitchel, and N. C. Fernelius in Beam- Solid Interactions for Materials Synthesis and Characterization, edited by D. C. Jacobson, D. E. Luzzi, T. F. Heinz, and M. Iwaki, Mater. Res. Soc. Proc. 354, (Pittsburgh, PA, 1994), pp. 729-734.

2. P. G. Schunemann, P. J. Drevinsky, and M. C. Ohmer in Beam-Solid Interactions for Materials Synthesis and Characterization, edited by D. C. Jacobson, D. E. Luzzi, T. F. Heinz, and M. Iwaki, Mater. Res. Soc. Proc. 354, (Pittsburgh, PA, 1994) pp. 579-583.

3. M. H. Rakowsky, W. K Kuhn, W. J. Lauderdale, L. E. Halliburton, G. J. Edwards, M. P. Scripsick, P. G. Schunemann, T. M. Pollak, M. C. Ohmer, and F. K. Hopkins, Appl. Phys. Lett. 64, 1615 (1994).

4. N. C. Giles, L. E. Halliburton, P. G. Schunemann, and T. M. Pollak, Appl. Phys. Lett. 66, 1758 (1995).

5. U. Kaufmann, J. Schneider, and A. Räuber, Appl. Phys. Lett. 29, 312 (1976).

6. S. D. Setzler, N. C. Giles, L. E. Halliburton, P. G. Schunemann, and T. M. Pollak, submitted to Applied Physics Letters.

7. L. E. Halliburton, G. J. Edwards, M. P. Scripsick, M. P. Rakowsky, P. G. Schunemann, and T. M. Pollak, Appl. Phys. Lett. 66, 2670 (1995).

8. N. Dietz, I. Tsveybak, W. Ruderman, G. Wood, and K. J. Bachmann, Appl. Phys. Lett. 65, 2759 (1994).

9. J. E. McCrae, Jr., M. R. Gregg, R. L. Hengehold, Y. K. Yeo, P. H. Ostdiek, M. C. Ohmer, P. G. Schunemann, and T. M. Pollak, Appl. Phys. Lett. 64, 3142 (1994).

10. N. P. Baran, I. I. Tychina, I. G. Tregub, I. Yu. Tkachuk, L. I. Chernenko, and I. P. Shcherbyna, Sov. Phys. Semicond. 9, 1527 (1976).

11. Dr. Keith J. Nash, DERA, Malvern, United Kingdom (private communication).

12. P. G. Schunemann and T. H. Pollak, MRS Bulletin 23, 23 (1998).

13. K. T. Stevens, S. D. Setzler, L. E. Halliburton, N. C. Fernelius, P. G. Schunemann, and T. M. Pollak, Mater. Res. Soc. Proc. 484, (Pittsburgh, PA, 1994), pp. 549-554.

14. H. J. Sun, C. F. Rong, and G. D. Watkins, Phys. Rev. B 50, 10619 (1994).

15. P. G. Schunemann in *Conf. on Lasers and Electro-Optics*, 1996 OSA Technical Digest Ser., vol. 9 (Optical Society of America, Washington, DC, 1996) p. 230.

16. G. W. Iseler, H. Kildal, and N. Menyuk, J. Electron. Mater. 7, 737 (1978).

17. D. W. Fischer, M. C. Ohmer, and J. E. McCrae, J. Appl. Phys. 81, 3579 (1997).

18. B. H. Bairamov, V. Yu. Rud', and Yu. V. Rud', in *MRS Bulletin* vol. 23(7) (Mater. Res. Soc., Pittsburgh, PA, 1998) p.41.

19. See, for example, N. W. Ashcroft and N. D. Mermin, *Solid State Physics* (Saunders College Publishers, New York, 1976), p. 586.

20. See, for example, R. H. Bube, *Electronic Properties of Crystalline Solids* (Academic Press, New York, 1974), p.364.

21. See, for example, J. P. McKelvey, *Solid State Physics for Engineering and Materials Science* (Krieger Publishing Company, Malabar, Florida, 1993), p. 388.

22. S. I. Borisenko and G. F. Karavaev, Izv. Vyssh. Uchebn. Zaved., Fiz. 1, 68 (1982).

23. See, for example, R. H. Bube, *Electronic Properties of Crystalline Solids* (Academic Press, New York, 1974), p.311.

24. P. F. Bordui and M. M. Fejer, Annu. Rev. Mater. Sci. 23, 321 (1993)

25. W. Koechner, Solid-State Laser Engineering, Fourth Edition, (Springer-Verlag, Berlin, 1996).

26. V. G. Dmitriev, G. G. Gurzadyan, and D. N. Nikogosyan, Handbook of Nonlinear Optical Crystals, Second Edition, (Springer-Verlag, Berlin, 1997).

27. M. G. Roelofs, J. Appl. Phys. 65, 4976 (1989).

28. G. M. Loiacono, D. N. Loiacono, T. McGee, and M. Babb, J. Appl. Phys. 72, 2705 (1992).

29. R. Blachman, P. F. Bordui, and M. M. Fejer, Appl. Phys. Lett. 64, 1318 (1994).

30. B. Boulanger, M. M. Fejer, R. Blachman, and P. F. Bordui, Appl. Phys. Lett. 65, 2401 (1994).

31. M. P. Scripsick, D. N. LoIacono, J. Rottenberg, S. H. Goellner, L. E. Halliburton, and F. K. Hopkins, Appl. Phys. Lett. 66, 3428 (1995).

32. J. P. Feve, B. Boulanger, G. Marnier, and H. Albrecht, Appl. Phys. Lett. 70, 277 (1997).

33. P. A. Thomas, A. M. Glazer, and B. E. Watts, Acta. Cryst. B46, 333 (1990).

34. G. J. Edwards, M. P. Scripsick, L. E. Halliburton, and R. F. Belt, Phys. Rev. B 48, 6884 (1993).

35. N. M. Nizamutdinov, N. M. Khasanova, G. R. Bulka, V. M. Vinokurov, I. S. Rez, V. M. Garmash, and N. I. Pavlova, Sov. Phys. Crystallogr. 32, 408 (1987).

36. J. F. Stenger, Y. Dusausoy, G. Marnier, H. Rager, and J. M. Gaite, J. Phys.: Condens. Matter 1, 4643 (1989).

37. J. M. Gaite, J. F. Stenger, Y. Dusausoy, G. Marnier, and H. Rager, J. Phys.: Condens. Matter 3, 7877 (1991).

38. M. P. Scripsick, G. J. Edwards, L. E. Halliburton, R. F. Belt, and G. M. Loiacono, J. Appl. Phys. 76, 773 (1994).

39. S. D. Setzler, G. J. Edwards, K. T. Stevens, L. E. Halliburton, M. P. Scripsick, and N. C. Fernelius, Phys. Rev. B (submitted).

40. M. P. Scripsick, G. J. Edwards, L. E. Halliburton, R. F. Belt, J. Appl. Phys. 70, 2991 (1991).

41. M. P. Scripsick, G. J. Edwards, L. E. Halliburton, R. F. Belt, and L. A. Kappers, SPIE Proceedings, Vol. 1561, pp. 93-103 (1991).

42. E. Simanek, Z. Sroubek, K. Zdansky, J. Kaczer, and L. Novak, Phys. Stat. Sol. 14, 333 (1966).

43. A. Raizman, A. Schoenberg, and J. T. Suss, Phys. Rev. B 20, 1863 (1979).

44. W. L. Warren, B. A. Tuttle, B. N. Sun, Y. Huang, and D. A. Payne, Appl. Phys. Lett. 62, 146 (1993).

45. M. A. Laruhin, V. N. Efimov, and V. A. Nazarova, Appl. Magn. Reson. 12, 517 (1997).

46. L. G. Karaseva, B. V. Andreev, V. V. Gromov, B. N. Zakharkin, and N. I. Pavlova, Akad. Nauk. Dokl. SSSR 289, 1152 (1986).

47. P. W. M. Jacobs, E. A. Kotomin, A. Stashans, E. V. Stefanovich, and I. Tale, J. Phys.: Condens. Matter 4, 7531 (1992).

48. W. E. Hughes and W. G. Moulton, J. Chem. Phys. 39, 1359 (1963).

49. S. W. Ahn, S. H. Choh, and J. N. Kim, J. Phys.: Condens. Matter 7, 667 (1995).

50. S. W. Ahn, S. H. Choh, and B. C. Choi, J. Phys.: Condens. Matter 7, 9615 (1995).

51. S. D. Setzler, Ph.D. dissertation, Department of Physics, West Virginia University, 1998.

52. R. H. D. Nuttall and J. A. Weil, Can. J. Phys. 59, 1696 (1981).

53. A. E. Hughes and B. Henderson, in Point Defects in Solids, edited by James H. Crawford, Jr. and Lawrence M. Slifkin (Plenum, New York, 1972), Vol. 1, Chap. 7, pp. 443-455.

54. R. Chen, in Thermoluminescence and Thermoluminescent Dosimetry, edited by Y. S. Horowitz (CRC Press, Boca Raton, 1984), Vol. 1, pp. 49-88.

55. R. Chen, J. Electrochem. Soc. 116, 1254 (1969).